Eruption of Shallow Crystal Cumulates during Explosive Phonolitic Eruptions on Tenerife, Canary Islands

Author(s):
Sliwinski, Jakub; Bachmann, Olivier; Ellis, Ben S.; Dávila-Harris, Pablo; Nelson, Bruce K.; Dufek, Josef

Publication date:
2015-11

Permanent link:
https://doi.org/10.3929/ethz-b-000108566

Originally published in:
Journal of Petrology 56(11), https://doi.org/10.1093/petrology/egv068

JOURNAL OF PETROLOGY

Journal of Petrology, 2015, Vol. 56, No. 11, 2173–2194
doi: 10.1093/petrology/egv068
Advance Access Publication Date: 15 December 2015
Original Article

OXFORD

Eruption of Shallow Crystal Cumulates during Explosive Phonolitic Eruptions on Tenerife, Canary Islands

J. T. Sliwinski[1]*, O. Bachmann[1], B. S. Ellis[1], P. Dávila-Harris[2], B. K. Nelson[3] & J. Dufek[4]

[1]Institute of Geochemistry and Petrology, ETH Zürich, Clausiusstrasse 25, 8092 Zürich, Switzerland; [2]Applied Geosciences Department, Instituto Potosino de Investigación Científica y Tecnológica, 78216 San Luis Potosí, Mexico; [3]Department of Earth and Space Sciences, University of Washington, Seattle, WA 98195, USA and [4]Department of Earth and Atmospheric Sciences, Georgia Institute of Technology, Atlanta, GA 30332, USA

*Corresponding author. Telephone: 041 78 705 8698. E-mail: jakub.sliwinski@erdw.ethz.ch

Received November 5, 2014; Accepted November 2, 2015

ABSTRACT

The recent eruptive history on the island of Tenerife is characterized in part by the presence of zoned phonolitic ignimbrites, some of which prominently display two types of juvenile clasts (i.e. light-colored, aphyric pumices alongside darker, more crystal-rich pumices, here dubbed 'crystal-poor' and 'crystal-rich', respectively). Petrographic observation of the crystal-rich pumices reveals intensely resorbed and intergrown mineral textures, consistent with the system reaching a high crystallinity, followed by perturbation and remobilization prior to eruption. Some trace elements show anomalous concentrations in such crystal-rich pumices (e.g. bulk Ba $>$ 2000 ppm alongside low Zr and a positive Eu anomaly) indicative of crystal accumulation (of feldspar $\pm$ biotite). Many biotite and feldspar crystals are reversely zoned, with rim concentrations that are high in Ba but low in Sr, implying crystallization from an 'enriched' melt, potentially derived from remobilization by partial melting of the aforementioned cumulate zones. Given (1) the presence of cumulates in the eruptive record on Tenerife and a bimodality of pumice textures, (2) the presence of three dominant compositions (basanite, phonotephrite, phonolite, separated by compositional gaps) in the volcanic record, and (3) abundant support for crystal fractionation as the dominant drive for magmatic evolution in Tenerife, it is hypothesized that crystal-poor magmas are extracted from mushy reservoirs in both the lower and upper crust. The thermodynamic software MELTS is used to test a polybaric differentiation model whereby phonolites (*sensu lato*) are generated by extraction of residual liquids from an intermediate-crystallinity phonotephritic mush in the upper crust, which is in turn generated from the residual liquids of an intermediate-crystallinity basanitic mush at deeper levels. Latent heat spikes following crystallization of successive phases in the upper crustal reservoir provide a thermal buffering mechanism to slow down cooling and crystallization, permitting enhanced melt extraction at a particular crystallinity interval (mostly $\sim$40–60 vol. % crystals). MELTS modeling typically fits the observed chemical data adequately, although some major elements (mostly Al_2O_3) also indicate partial 'cannibalization' of feldspar along with some magma mixing (and potentially minor crustal contamination).

Key words: alkaline magmatism; fractional crystallization; mineral chemistry; rhyolite-MELTS; Tenerife

INTRODUCTION

The generation of large volumes of silicic igneous rocks seen in the volcanic record remains a controversial topic in igneous petrology and is essential to our understanding of explosive volcanic eruptions. Differentiation of silicic magmas is a complex physico-chemical process that may entail partial melting of pre-existing crustal rocks, fractional crystallization of mafic parents, or some combination of both (assimilation–fractional crystallization, AFC; see Taylor, 1980; DePaolo, 1981). The evidence for each mechanism is often elusive and controversies surround their relative contributions to differentiation. At the same time, certain common traits such as petrographic and chemical zonation in ignimbrites (Lipman, 1966; Lipman & Mehnert, 1975; Hildreth, 1979; Wolff & Storey, 1984; Wörner & Schmincke, 1984; Bacon & Druitt, 1988; Bryan, 2006; Deering *et al.*, 2011) and compositional gaps in volcanic series (Bunsen, 1851; Daly, 1925; Chayes, 1963; Sigurdsson & Sparks, 1981; Brophy, 1991; Freundt-Malecha *et al.*, 2001) occur prominently and consistently throughout magmatic provinces around the world. Indeed, the prevalence of such gaps and chemical zonation in ignimbrites suggests that they are intrinsic to the process of differentiation and can help us shed light on controversies surrounding the mechanisms of magmatic evolution (Bachmann & Bergantz, 2004; Dufek & Bachmann, 2010; Szymanowski *et al.*, 2015).

Petrographic and/or chemical zoning patterns are prevalent in many ignimbrites on the island of Tenerife in the Canary Islands (Wolff & Storey, 1984; Wolff, 1985; Bryan *et al.*, 1998, 2002; Bryan, 2006). In particular, many units contain two or more varieties of juvenile clasts, including light-colored aphyric pumices, darker crystal-rich pumices (here referred to as 'crystal-poor' and 'crystal-rich,' respectively) as well as compositionally banded pumices. One question that arises from these observations is whether the crystal-rich and crystal-poor pumices are genetically related [see Bachmann *et al.* (2014) for such a case], and, if so, whether this genetic relationship provides a clue to how magmas evolve on Tenerife. Can this bimodality in crystallinity be in some ways related to the bulk-rock compositional gaps that are obvious in the volcanic record?

Geochemical models can be ideally implemented in provinces that are geochemically and tectonically well characterized, such as Tenerife (Ablay *et al.*, 1998; Neumann *et al.*, 1999; Thirlwall *et al.*, 2000; Wiesmaier *et al.*, 2012). Here, there exists a large geochemical database, a well-defined pyroclastic stratigraphy, a clear demonstration of compositional gaps, and a relatively simple geotectonic setting that minimizes the influence of heterogeneous crustal components on the magmas. In the event that a genetic relationship between crystal-rich and crystal-poor juvenile products can be demonstrated, geochemical modeling (using rhyolite-MELTS; hereafter referred to simply as MELTS; Gualda *et al.*, 2012) may provide constraints on the importance of this genetic process in the overall scheme of magmatic differentiation on Tenerife.

GEOLOGICAL SETTING

The Canary Islands lie 750 km west of the Moroccan coast and represent ~20 Myr of hotspot activity (Abdel-Monem *et al.*, 1971; Schmincke, 1976; Fig. 1). The alkaline volcanic chain extrudes through transitional oceanic–continental crust in the east (Fuerteventura and Lanzarote islands), and through ~7 km thick oceanic crust in the west, all of which are overlain by several kilometers of Africa-derived sediments (Robertson & Stillman, 1979; Hoernle, 1998; Ye *et al.*, 1999). Active seismic tomography on the nearby island of Gran Canaria indicates that the Moho is located at ~15 km depth relative to sea level (Krastel & Schmincke, 2002) and geobarometric constraints suggest that magma pooling at this discontinuity may represent layered magma reservoirs beneath the Canary Islands (Hoernle *et al.*, 1991; Ablay *et al.*, 1998; Klügel *et al.*, 2005). Extensive magmatic differentiation sometimes produces phonolitic to trachytic eruptions following the initial shield-building stages (Wolff, 1987; Carracedo, 1999). This is seen most prominently on the islands of Gran Canaria and Tenerife.

The island of Tenerife is situated near the center of the archipelago and represents >11·6 Myr of eruptive history, which began with the eruption of the Teno, Anaga and Roques del Conde basanitic shields (Fig. 1) and progressed to more felsic activity at ~3 Ma with the building of the Las Cañadas Volcanic Edifice (LCVE; Martí *et al.*, 1994; Ancochea *et al.*, 1999; Thirlwall *et al.*, 2000). Whereas the LCVE erupted abundant volumes of both mafic and felsic products in its early stages, it later changed to more evolved volcanism (Araña & Brändle, 1969; Bryan *et al.*, 1998; Ancochea *et al.*, 1999), depositing a sequence of phonolitic ignimbrites and fall deposits, which are very well exposed on the southern flanks of the island (the Bandas del Sur pyroclastic apron). These have been the focus of numerous stratigraphic studies (Bryan *et al.*, 1998, 2002; Edgar *et al.*, 2002; Brown *et al.*, 2003; Bryan, 2006; Edgar *et al.*, 2007; Dávila-Harris, 2009; Dávila-Harris *et al.*, 2013) and are the topic of this study. Meanwhile, three radial rift zones are the sources of voluminous basaltic to phonotephritic lava flows, which are integral to the construction and, following overgrowth and lateral collapse, destruction of parts of the island (Fig. 1; Carracedo, 1994; Carracedo *et al.*, 2007, 2011).

The later silicic volcanism of the LCVE has been historically subdivided into three eruptive cycles, each separated by an ~100 kyr hiatus and comprising many subordinate plinian–subplinian eruptions (0–20 km^3 dense rock equivalent volume; see Martí *et al.*, 1994; Bryan *et al.*, 1998; Edgar *et al.*, 2007). These eruptions are spaced tens of thousands of years apart and typically overlie paleosol horizons. Here, we study five well-exposed zoned ignimbrites: the Gaviotas

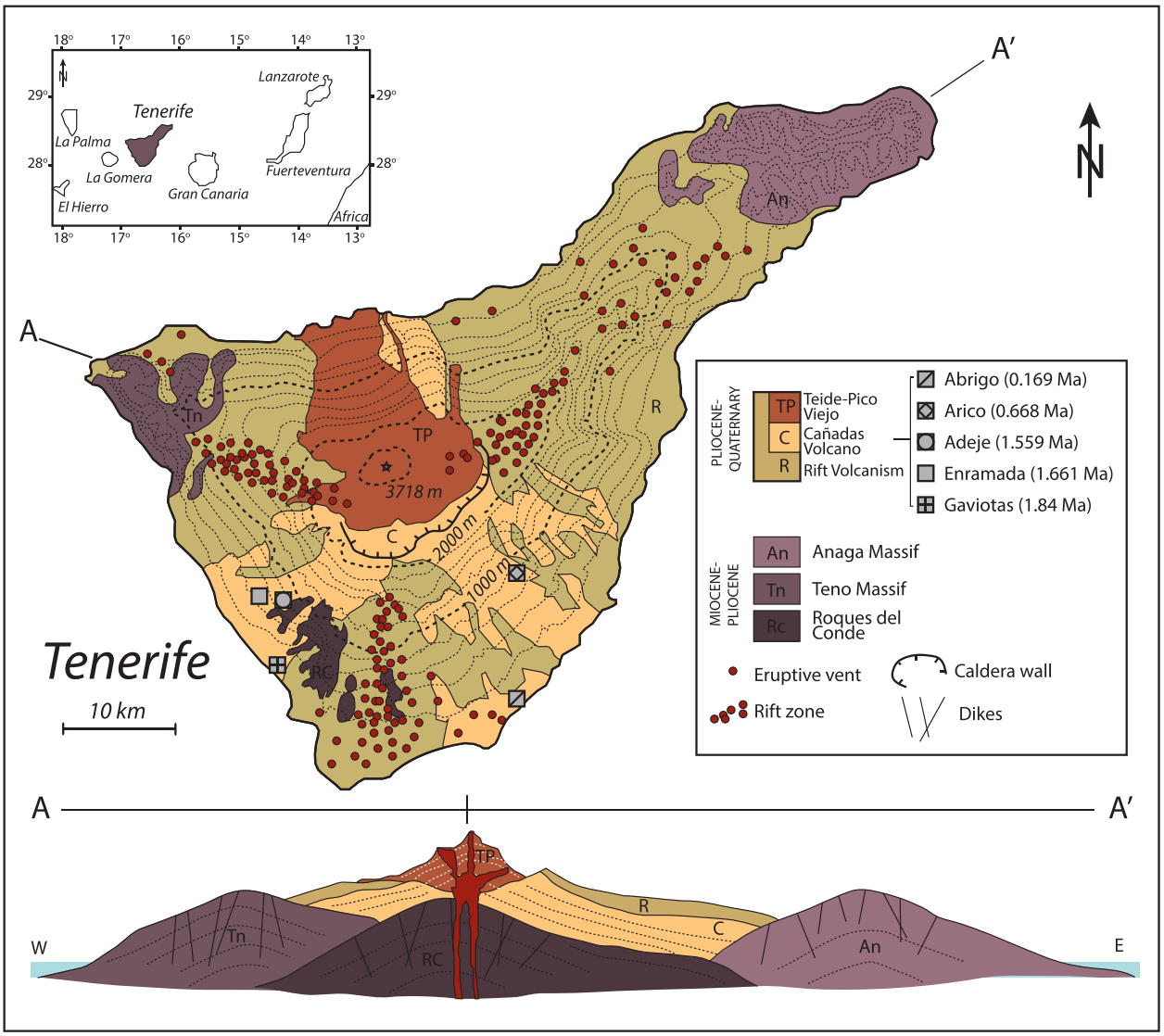

Fig. 1. Simplified geological map of Tenerife with major geological features: three overlapping basanitic shields (Roques del Conde, Teno and Anaga) unconformably overlain by products from the Las Cañadas volcano and the Teide–Pico Viejo Complex, concurrent with rift volcanism. Gaviotas, Enramada, Adeje, Arico and El Abrigo ignimbrites are shown in schematic stratigraphic order and patterned squares represent sampling locations. Inset: Canary Islands. Modified after Carracedo *et al.* (2007).

(1·84 ± 0·07 Ma), Enramada (1·661 ± 0·02 Ma), Adeje (1·559 ± 0·014 Ma), Arico (0·668 ± 0·004 Ma) and El Abrigo (0·169 ± 0·001 Ma) ignimbrites (Bryan *et al.*, 1998; Huertas *et al.*, 2002; Brown *et al.*, 2003; Dávila-Harris, 2009; Dávila-Harris *et al.*, 2013).

METHODS

Sampling and database management

Many volcanic units on Tenerife have been extensively sampled over the last decades by numerous groups and chemical data are accessible from many sources (Ridley, 1970; Brändle & Santín, 1979; Neumann *et al.*, 1999; Thirlwall *et al.*, 2000; Nichols, 2001; Edgar *et al.*, 2002, 2007; Bryan, 2006; Gurenko *et al.*, 2006; Dávila-Harris, 2009). Whole-rock major and trace element data for the entire range of Tenerife volcanic products were obtained from the GEOROC database (Sarbas & Nohl, 2008) in October 2012 and screened to exclude any analyses below 99 total wt %, totaling 824 analyses. For simplicity, only a representative subset of these data are plotted. This subset includes: mafic lavas from Thirlwall *et al.* (2000); syenites, banded, mafic and aphyric pumices from Nichols (2001) and Edgar *et al.* (2007); crystal-rich pumices and other phonolites from Dávila-Harris (2009); and crystal-rich and crystal-poor pumices (this study).

To gain a mineral-scale understanding of magmatic processes, juvenile clasts were collected during a 2012 field campaign from both the SE and SW Bandas del Sur pyroclastic apron (Fig. 1; Supplementary Material S1; supplementary data are available for downloading at http://www.petrology.oxfordjournals.org) following the stratigraphy outlined by Brown *et al.* (2003) and

Dávila-Harris (2009). Five ignimbrites were selected that feature crystal-rich pumices (the Gaviotas, Enramada, Adeje, Arico and El Abrigo Formations), and special attention was paid to samples such as unusual juvenile clasts, along with lighter colored aphyric pumices. In all, 31 unaltered tephriphonolitic to phonolitic pumices, representing the five ignimbrites, were chosen for petrographic studies, and whole-rock and mineral chemical analysis.

Whole-rock geochemistry

Fused whole-rock XRF beads (1:5 lithium tetraborate dilution) were prepared and analyzed at ETH Zürich using a PANalytical Axios wavelength-dispersive X-ray fluorescence (WD-XRF) spectrometer following a 2 h devolatilization period at 900°C. Loss on ignition (LOI) was calculated as the difference between the weight of the original 1·6 g sample and the sample after devolatilization.

Mineral and glass major element chemistry

Major element concentrations in feldspar, glass and biotite were obtained by electron probe microanalysis (EPMA) at ETH Zürich (JEOL JXA-8200 for feldspar and glass) and Universität Kiel (JEOL JXA-8900 R for biotite). Standards from the ETH standard library were reproducible to 0–2 relative wt %. Feldspar, glass and biotite were analyzed with a 20 μm (feldspar and glass) or focused (biotite) beam for 20, 20 and 7 s on peaks and 20, 20 and 15 s for total background, respectively, using a 15 kV acceleration voltage and 20, 6 and 20 nA beam current, respectively. Feldspar and biotite analyses were normalized to 8 and 22 O per formula unit (respectively) using a Phi-Rho-Z correction scheme and monitored with the Smithsonian NMNH143965 Kakanui hornblende and NMNH143966 microcline (Jarosewich *et al.*, 1980), as well as ETH's albite, anorthite, clinopyroxene and amphibole secondary standards.

Trace elements

Trace elements and rare earth elements (REE) in feldspar, biotite, glass and whole-rock beads were obtained by laser ablation inductively coupled plasma mass spectrometry (LA-ICP-MS) at ETH Zürich. Trace element abundances in glass were obtained from 100 μm thick sections for the Enramada, Adeje, Arico and El Abrigo units, and from epoxy mounts for the Gaviotas unit. Feldspar was analyzed in the same thin sections as glass, whereas biotite was analyzed exclusively in grain mounts owing to its lower modal abundance. For XRF pills, we used a 193 nm Lambda Physik excimer ArF laser coupled to a PerkinElmer ELAN 6100 ICP-MS system. Analyses were calibrated and drift-corrected using the NIST-610 synthetic glass standard and blank corrected using a lithium tetraborate blank. Spot sizes were 90 μm (lithium tetraborate blank) and 40 μm (sample), and an average of two or three points were taken per sample. For mineral and glass analyses, a 193 nm Resonetics ArF excimer laser paired with a Thermo Element XR ICP-MS system was utilized. Spot sizes were 30 μm (biotite), 43 μm (glass) and 67 μm (feldspar), typical output energy was 3·5 J cm^{-2} and the analyses were standardized and drift-corrected with the NIST-612 synthetic glass standard. Internal calibration was performed using as a secondary standard the SiO_2 content of the USGS GSD-1G synthetic glass standard.

Typical standardization and drift correction procedures consisted of bracketing 30 samples with four primary standards (NIST-610 or NIST-612; two before and two after), as well as analyzing one secondary standard per 30 analyses (GSD-1G for minerals or glass or lithium tetraborate blank for XRF pills). Trace element abundances were calculated for minerals and glass using the SiO_2 concentrations previously obtained by EPMA for internal standardization. Whole-rock concentrations were calculated with the lithium tetraborate blank and the SiO_2 content previously measured by WD-XRF. Drift correction and data reduction were carried out with the MATLAB-based SILLS software (Guillong *et al.*, 2008). Analytical error for single spots is difficult to quantify, but long-term laboratory reproducibility of homogeneous glass standards yields a precision significantly better than 5 relative % for elements with concentrations far above the limit of detection.

RESULTS

Petrography

Crystal-rich phonolitic pumices often include crystal aggregates and contain between 20 and 50% phenocrysts in thin section with a diverse, intergrown mineral assemblage consisting of 50–90% alkali feldspar (Table 1). Biotite and pyroxene are common and together can form up to 15% of the mineral assemblage, and less abundant phases include plagioclase (typically absent but occasionally $>20\%$) + Fe–Ti oxides (magnetite ± ilmenite forming 1–5%) + haüyne/sodalite (1–5%) + apatite (as inclusions in biotite and pyroxene) ± titanite (1–3%) ± amphibole. Pumices typically have a glassy groundmass and are 15–60% vesiculated. Microlite content is usually low, with the exception of the Gaviotas unit, where feldspar and amphibole microlites form the majority of the groundmass. Crystal aggregates are common within crystal-rich pumices, occurring as either (1) disaggregated crystals that preserve the shapes of previously attached crystals, (2) felsic and mafic aggregates measuring <1 mm to 1 cm (Fig. 2a and b), or (3) large pods of aggregated crystals >1 cm (Fig. 2e and f; Supplementary Material S2).

Alkali feldspar in crystal-rich pumices ranges from <100 μm to >1 cm, occurs either in crystal clusters or alone, and commonly shows moderate to severe resorption, embayed textures and patchy zoning (Fig. 2d–f, Supplementary Material S2). Where resorbed, some feldspar occasionally shows interstitial recrystallization of oxides and amphibole, typically alongside wormy cores visible in backscatter electron (BSE) images

Table 1: Phenocryst modal abundances in petrographic thin sections

Sample:	001	005	007	010	011	015	019	020	029	031	043	047	049*	053	054	055	057
Unit:†	Enr	Enr	Enr	Adj	Adj	Adj	Gav	Gav	Ari	Ari	Abr	Abr	Abr	Abr	Abr	Abr	Abr
Crystallinity:‡	15·7	28·2	19·1	26·2	12·8	17·1	31·0	19·6	10·0	10·9	47·2	21·7	17·0	25·8	23·4	40·4	25·1
n:	1286	2131	1881	1749	1892	1988	2105	933	1872	1798	2166	1696	2049	2011	1800	1805	1966
Vesicle %:	51·3	27·5	58·0	49·5	3·2	35·1	17·8	25·2	17·5	42·1	22·7	50·8	27·9	39·0	38·5	26·6	32·9
No. of phx§	98	436	151	232	235	221	653	137	154	113	791	181	251	316	259	535	336
kspar %	87·8	94·3	83·4	78·9	52·3	85·1	68·8	82·5	78·6	78·8	80·3	89·0	68·1	75·6	84·2	81·5	82·1
plag %	—	1·6	3·3	15·1	22·1	—	22·7	3·6	1·3	tr	3·5	—	4·0	—	0·8	—	—
px %	1·0	1·6	—	2·2	3·8	10·0	2·0	1·5	5·8	3·5	3·8	3·3	15·5	6·6	3·1	1·3	3·0
bt %	6·1	0·9	9·9	1·3	13·6	0·5	0·8	2·9	7·1	8·0	5·7	1·7	1·6	6·0	3·1	7·1	3·9
haü %	—	—	0·7	0·4	—	—	0·5	—	1·3	4·4	3·0	2·2	0·4	6·6	3·9	1·3	5·1
ap %	tr	tr	—	tr	1·7	tr	0·3	5·1	1·3	0·0	tr	tr	0·8	—	tr	0·9	0·3
ox %	5·1	1·1	2·6	2·2	6·0	3·2	2·6	2·2	4·5	5·3	1·4	3·9	8·0	5·1	5·0	2·2	5·7
tit %	—	0·5	—	tr	0·4	1·4	0·5	2·2	—	tr	2·3	tr	1·6	—	tr	5·6	tr
amp %	—	—	—	—	tr	tr	2·0	tr	—	tr	tr	—	—	—	—	—	—

*Very mingled clast.
†Enr, Enramada; Adj, Adeje; Ari, Arico; Abr, El Abrigo; Gav, Gaviota.
‡Crystallinity calculated as proportion of phenocrysts to phenocrysts and groundmass.
§phx, phenocryst; gms, groundmass; kspar, alkali feldspar; plag, plagioclase; px, pyroxene; bt, biotite; haü, haüyne; ap, apatite; ox, Fe–Ti oxides; tit, titanite; amp, amphibole.
n, number of points counted; tr, phase observed in trace quantities.

(Fig. 3c). Reverse zoning is often visible as bright, Ba-rich rims, typically showing higher anorthite content (Fig. 3a–c). Large glomerocrysts of feldspar are common and are sometimes intergrown with biotite ± haüyne or, less frequently, pyroxenes and oxides (Fig. 2a–f).

Biotite ranges from 100 μm to 2 mm in size, displays a euhedral to elongated habit and is usually only slightly (although occasionally severely) resorbed. Some phenocrysts show wormy resorption patterns and are often overgrown by fresh rims that appear much brighter in BSE (Fig. 3d–f). Multiple zones and zone reversals are most commonly seen in the Arico, Adeje and El Abrigo units, whereas Enramada and Gaviotas biotite crystals have relatively simple textures. Inclusions of apatite, oxides and melt are very common in biotite.

Other mafic phases (pyroxene, amphibole, Fe–Ti oxides, apatite, titanite, sulfides) usually show slight resorption with rounded edges, and often occur in small (<1 mm) aggregates with each other and occasionally with alkali feldspar or plagioclase (Fig. 2a and b). Samples from the Gaviotas unit contain abundant mafic glomerocrysts, whereas in other units their presence is mostly restricted to mingled mafic bands.

Bulk-rock geochemistry

Crystal-rich and crystal-poor pumices have very similar major element compositions [i.e. when compared on a total alkalis–silica (TAS) diagram] and are concordant with literature data, ranging from 57 to 64 wt % SiO_2 and from 11 to 15 wt % total alkali content (Table 2; Fig. 4). The majority of samples are phonolites or trachytes (*sensu stricto*) with one mingled sample classified as a tephriphonolite. They are shown as 'evolved' compositions in Fig. 5. Crystal-poor pumices are mildly depleted in MgO, FeO, TiO_2 and P_2O_5 relative to crystal-rich pumices, but contain comparable amounts of Al_2O_3, CaO, MnO, SiO_2, Na_2O and K_2O. There is no correlation between alkali content and age of sample, or between alkali content and LOI.

Compared with mafic to intermediate lavas, many crystal-rich phonolitic pumices are enriched in Ba, depleted in Sr and display Zr contents that are negatively correlated with Ba (Fig. 5). Crystal-poor pumices are strongly depleted in both Ba and Sr, and highly enriched in Zr (>1000 ppm). Trace element and REE patterns in crystal-poor pumices and syenites (normalized to primitive mantle; McDonough & Sun, 1995) indicate depletion in Ba, Sr and Eu alongside enrichment in Rb, Nb and Zr (Nichols, 2001; Fig. 6) compared with crystal-rich pumices. Samples described as banded and mafic pumices by Nichols (2001) and crystal-rich pumices (this study) are characterized by enrichment in Ba correlated with a positive Eu anomaly and depletion in Zr (Fig. 6, inset) relative to crystal-poor pumices.

Mineral and glass chemistry

Feldspar

Compositionally zoned alkali feldspar is observed in BSE images and appears in the Arico, El Abrigo, Adeje and Gaviotas units, most prominently in the Arico (see Supplementary Material S3). Most alkali feldspar in this study is classified as anorthoclase, with composition $An_{0–10}Or_{10–140}Ab_{60–180}$ (Table 3; Fig. 7a). El Abrigo feldspars are notably Or-rich (anorthoclase–sanidine), whereas those of the Gaviotas and Adeje are more calcic (anorthoclase–oligoclase). Whereas the majority of feldspar in the Enramada and Gaviotas units is unzoned and contains 100–4000 ppm Ba, the Arico, Adeje and El Abrigo units have subsets of feldspar with >5000 ppm Ba, which are reversely zoned (high-Ba calcic rims; Figs 3 and 7b). Feldspar crystals in the Arico and Adeje units are notable for strong reverse zoning in Ba,

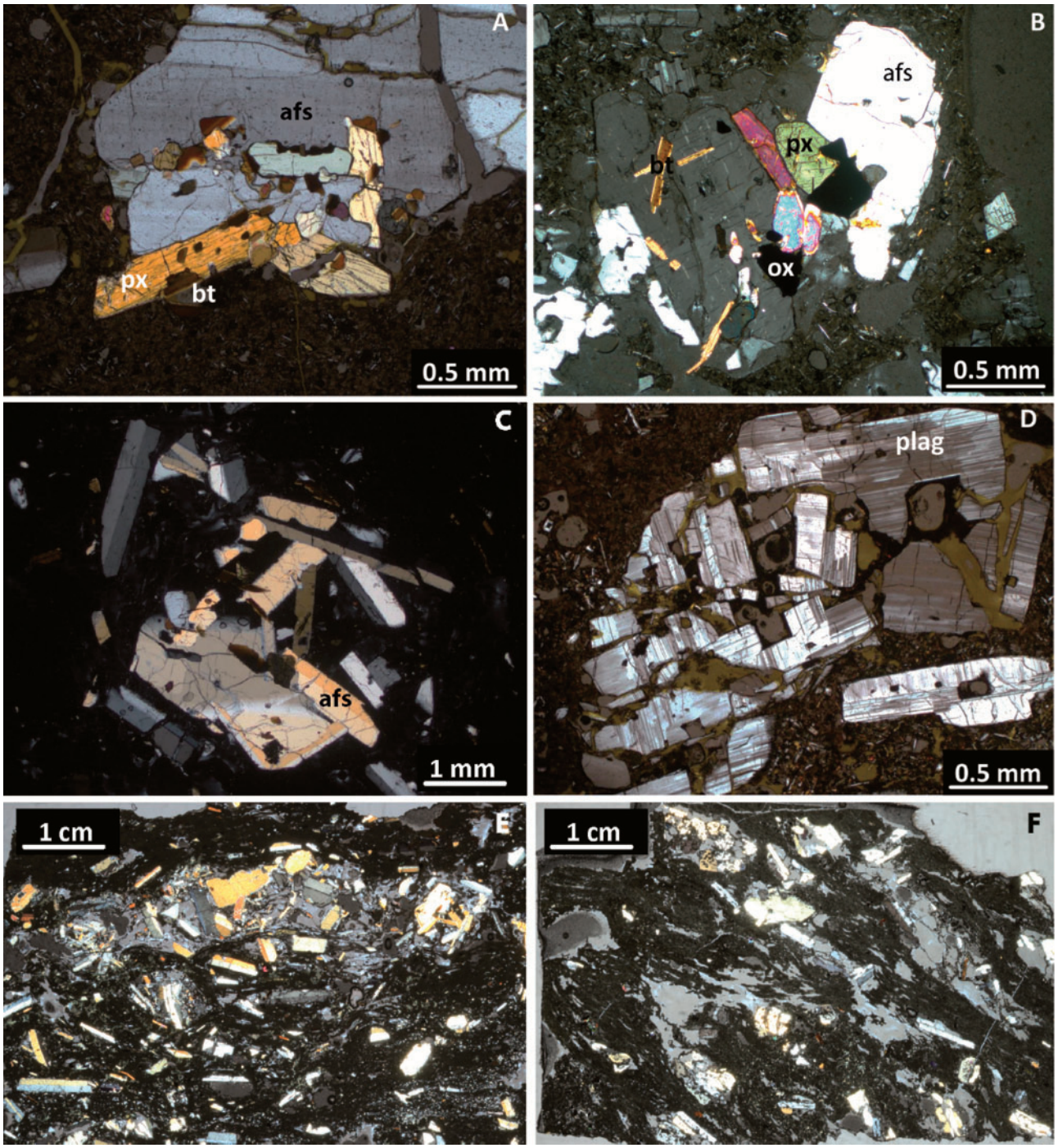

Fig. 2. Representative thin section photomicrographs of glomerocrysts from the Gaviotas Formation (a, b, d) and El Abrigo Formation (c, e, f): (a, b) intergrown alkali feldspar, pyroxene, oxides and biotite ± apatite (TFE_12_019, 20); (c) intergrown, slightly resorbed alkali feldspar glomerocryst (TFE_12_055); (d) plagioclase glomerocryst showing variable crystallographic orientations and partial resorbtion (TFE_12_019); (e) thin section demonstrating partly disaggregated glomerocryst (center; TFE_12_055); (f) cross-polarized light photomicrograph of pumice with multiple alkali feldspar glomerocrysts (particularly top left, bottom left to bottom right; TFE_12_054). afs, alkali feldspar; pl, plagioclase; px, augite; bt, biotite; ox, oxides; classification following Whitney & Evans (2010).

showing rims with up to ~15 000 ppm Ba. Sr content is positively correlated with Ba and is typically <1000 ppm in all units (<100 ppm in the Enramada), with Arico feldspar crystals showing exceptionally low values (<400 ppm; Fig. 7c).

Biotite

Biotite crystals are often compositionally zoned like the feldspars, with bright zones visible in BSE images that are strongly correlated with Ba content (Supplementary Material S3). All biotite is classified as phlogopite with

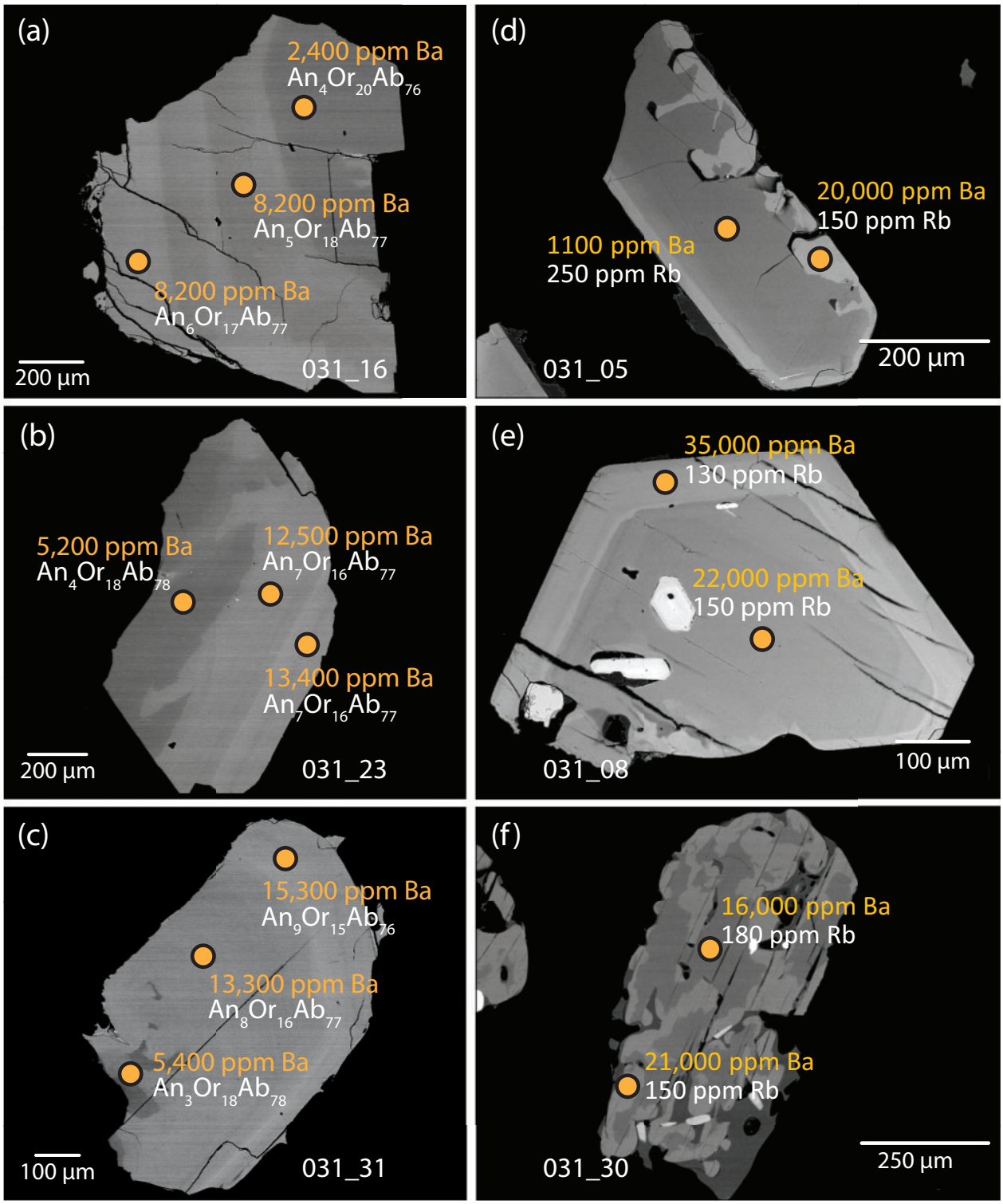

Fig. 3. (a–c) Backscattered electron (BSE) images of reversely zoned feldspars from the Arico unit, showing high enrichment in Ba from core and rim, and associated minor increases in An# and decreases in Or#; (d–f) BSE images of zoned biotite phenocrysts, showing extreme Ba variations between core and rim, together with a concurrent decrease in Rb. The prominent resorption in many phenocrysts should be noted. All grains are from sample TFE_12_031.

Mg# [Mg/(Mg + Fe)] from 60 to 76 and low Al (generally < 2·6 atoms per formula unit and inversely related to Mg; Table 3; Fig. 8a). Major element zonation is slight or absent, whereas zonation in Ba is pronounced in most units, sometimes approaching 25 000 ppm (Figs 3d–f and 8b). Rb varies between 100 and 500 ppm, and is inversely proportional to Ba content (Fig. 8c).

Table 2: Major and trace element bulk-rock XRF data for selected Tenerife ignimbrites

Sample:	001	002	007	009	010	015	017	018	019	020	022	023	023_2	024	031
Unit:	Enr	Enr	Enr	Adj	Adj	Adj	Mor	Mor	Gav	Gav	Gav	Gav	Gav	Gav	Ari
Texture:	xr	xr	xr	xr	xr	xr	xp	xp	xr	xr	xr	xr	xr	xr	xr
Major elements (wt %)															
SiO_2	62·45	62·87	63·58	62·00	61·17	60·43	63·67	62·02	60·08	58·81	59·11	58·03	58·54	58·98	61·52
TiO_2	0·80	0·82	0·82	0·92	1·02	0·87	0·79	0·76	0·85	1·12	1·08	1·13	1·11	1·07	0·85
Al_2O_3	17·34	17·38	17·73	17·96	17·99	17·49	17·33	16·91	19·10	19·29	19·21	19·24	19·06	19·26	18·29
FeO_T*	2·86	2·96	2·90	3·33	3·55	3·06	3·27	3·62	3·05	3·84	3·71	3·82	3·71	3·70	3·10
CaO	0·78	1·49	0·80	1·57	1·98	4·04	1·00	1·33	1·67	3·05	2·78	4·21	3·50	2·93	0·98
MgO	0·63	0·60	0·58	0·98	1·08	0·84	0·56	0·40	0·64	0·98	1·12	1·21	1·11	0·94	0·81
MnO	0·16	0·17	0·16	0·18	0·17	0·17	0·23	0·28	0·18	0·18	0·18	0·18	0·18	0·18	0·21
K_2O	5·35	5·43	5·37	4·19	3·99	4·15	5·47	5·32	4·98	4·14	4·30	3·87	4·15	4·30	4·87
Na_2O	7·58	7·62	7·78	7·95	7·96	8·11	7·53	8·85	8·31	7·67	7·71	7·47	7·64	7·81	8·91
P_2O_5	0·17	0·17	0·17	0·22	0·26	0·20	0·08	0·06	0·13	0·23	0·26	0·37	0·30	0·22	0·16
Total	98·4	100·0	100·34	99·7	99·6	100·00	100·49	100·20	99·3	100·08	100·18	99·9	100·01	100·11	100·05
Trace elements (ppm)															
Ba	351	222	388	1558	1775	1694	12	52	574	910	832	940	924	799	1578
Sr	10	11	9	239	438	274	15	15	287	633	583	757	612	599	30
Zr	320	371	335	446	386	392	713	1097	1039	775	810	708	750	831	564
Rb	64	71	68	71	62	67	110	142	144	110	112	98	106	115	87
V	27	32	32	29	36	26	34	28	31	52	51	52	53	51	42
Sc	4	3	3	0	3	3	1	4	1	5	5	5	2	1	2
Cr	3	3	1	0	3	2	3	3	3	7	11	1	3	0	1
Co	4	4	2	4	3	0	3	2	4	5	5	10	6	4	2
Ni	6	8	5	16	9	9	9	9	11	7	15	7	8	7	8
Cu	20	6	1	18	28	4	6	6	28	4	8	17	6	5	10
Zn	83	92	87	105	94	99	127	165	105	106	105	102	103	105	115
Y	30	35	32	37	34	35	57	75	46	43	43	40	42	43	37
Nb	86	98	90	108	98	98	183	248	213	171	174	160	166	180	151
La	75	85	83	80	66	71	142	162	116	104	95	88	93	96	118
Hf	—	14	12	—	—	16	25	36	—	30	30	—	29	29	—
Th	4	8	8	9	6	8	15	23	18	16	16	13	16	18	15
U	0	1	0	1	0	0	3	3	2	1	0	0	0	1	3

Sample:	032	036	043	044	045	046	047	048	049	050	051	053	054	055	057	059	065
Unit:	Ari	Abr	Abr	Abr	Abr	Abr	Abr	Abr	Abr	Abr	Abr	Abr	Abr	Abr	Abr	Abr	Enr
Texture:	xr	xr	bp	xr	xp	xp	xr	xr	xr	xp	xr	xr	xr	xr	xr	xr	xp
Major elements (wt %)																	
SiO_2	61·45	59·02	60·05	55·38	57·24	57·73	60·70	60·50	57·30	58·57	60·28	61·40	60·34	59·40	61·43	59·29	63·56
TiO_2	0·89	0·89	1·02	1·71	0·61	0·74	0·79	0·86	1·40	0·74	1·08	0·86	0·89	0·75	0·84	0·98	0·60
Al_2O_3	18·34	18·32	19·07	18·93	20·27	19·73	18·55	18·69	18·36	18·71	18·71	18·56	18·63	18·90	18·59	18·46	16·28
FeO_T	3·14	3·08	2·96	5·11	2·88	3·09	2·83	3·10	4·47	3·38	3·47	2·88	3·02	3·14	2·76	3·34	3·47
CaO	1·08	2·16	1·89	4·43	3·65	2·13	1·22	1·60	3·21	2·09	1·96	1·20	1·49	1·50	1·58	2·90	2·53
MgO	0·78	0·73	0·64	1·79	0·74	0·72	0·47	0·58	1·38	0·61	0·90	0·57	0·64	0·41	0·62	0·79	0·48
MnO	0·21	0·18	0·13	0·17	0·18	0·18	0·18	0·19	0·19	0·23	0·17	0·17	0·17	0·22	0·16	0·19	0·28
K_2O	4·76	5·11	5·74	4·33	5·49	5·41	5·71	5·47	4·56	5·51	5·05	5·64	5·27	5·66	5·58	5·20	4·90
Na_2O	8·96	8·37	7·54	7·19	8·61	8·59	8·56	8·73	7·95	8·94	8·03	8·24	8·37	9·37	8·17	8·46	7·21
P_2O_5	0·17	0·16	0·14	0·49	0·11	0·13	0·10	0·13	0·35	0·10	0·23	0·14	0·15	0·07	0·13	0·19	0·06
Total	100·12	98·7	99·5	100·47	100·35	99·1	99·6	100·45	100·0	99·3	100·55	100·15	99·6	100·02	100·36	100·44	99·8
Trace elements (ppm)																	
Ba	1704	1177	1384	1275	263	409	228	566	985	38	1276	451	1102	11	580	868	9
Sr	31	171	234	745	207	245	40	131	479	55	246	52	152	27	68	197	18
Zr	530	693	533	592	1199	1106	709	760	680	1306	547	540	613	1183	511	745	1205
Rb	83	107	98	92	184	178	118	121	99	178	89	94	101	168	91	114	161
V	43	50	61	119	39	49	42	48	86	46	61	44	47	44	42	54	26
Sc	0	2	0	4	0	0	0	2	0	2	2	3	0	1	0	2	2
Cr	4	7	2	7	6	11	4	32	1	9	0	3	6	3	1	0	3
Co	4	3	2	14	1	4	3	0	7	3	3	3	7	1	2	4	4
Ni	6	6	8	22	8	8	2	18	0	14	5	8	4	4	2	8	10
Cu	6	8	6	8	4	5	6	8	7	7	3	3	5	5	6	7	7
Zn	111	104	84	100	113	109	102	107	107	141	99	92	96	132	89	108	132
Y	36	39	47	42	32	35	37	40	42	55	36	33	35	53	32	44	66
Nb	145	158	166	152	200	190	166	177	156	263	130	130	144	254	124	168	265
La	109	97	120	86	105	114	104	119	102	144	97	105	103	145	96	107	186
Hf	—	—	—	—	—	—	—	—	—	—	19	—	—	—	—	25	—
Th	10	14	14	14	33	32	20	18	16	32	13	11	15	26	11	18	26
U	2	2	2	0	8	8	5	6	2	7	1	2	3	7	3	1	6

*FeO_T denotes total Fe as FeO.
Enr, Enramada; Adj, Adeje; Ari, Arico; Abr, El Abrigo; Gav, Gaviota; Mor, Morteros; Ce, Ga, Nd and Pb analyses excluded owing to poor standardization; xr, crystal-rich; xp, crystal-poor; bp, banded pumice.

Groundmass

The groundmass in crystal-rich pumices is typically glassy with the exception of the Gaviotas unit, where feldspar and amphibole microlites make up >95% of the groundmass. Glass is texturally homogeneous to slightly microcrystalline in most units and contains 59–64 wt % SiO_2, 17–20 wt % Al_2O_3, 7–11 wt % Na_2O, 4·5–6·5 wt % K_2O, 2–4 wt % FeO and 0–1 wt % MgO (Table 3; Fig. 9a). Sr and Ba contents vary widely between units, with either low-Sr–high-Ba (the Arico unit),

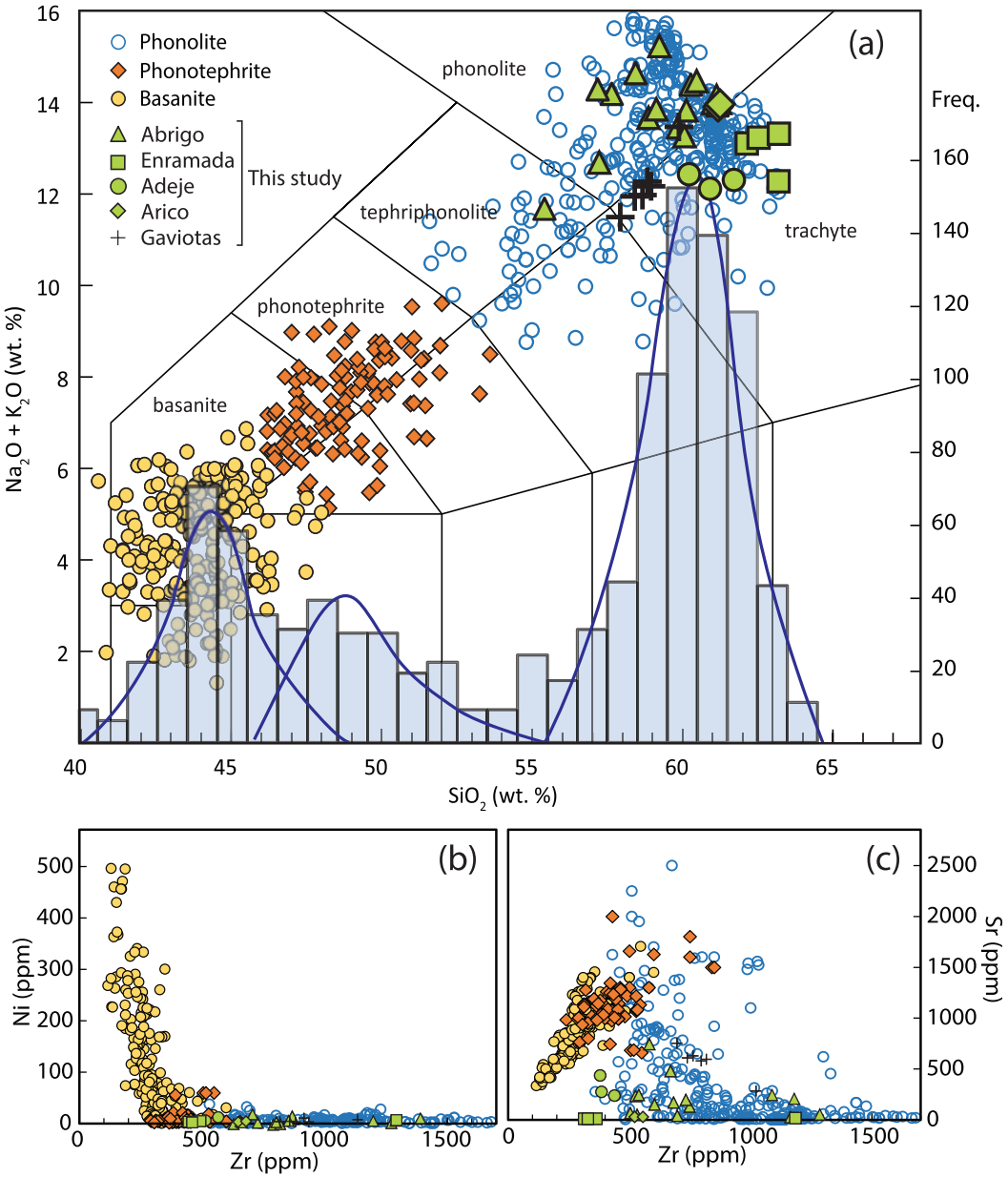

Fig. 4. (a) Bulk-rock TAS diagram for all studied Tenerife units following the classification scheme of Le Bas *et al.* (1986), showing literature data (basanites, phonolites and phonotephrites; $n = 874$; Araña & Brändle, 1969; Ibarrola, 1969; Ridley, 1970; Brändle & Santín, 1979; Ablay *et al.*, 1995, 1998; Neumann *et al.*, 1999; Thirlwall *et al.*, 2000; Wolff *et al.*, 2000; Nichols, 2001; Bryan *et al.*, 2002; Gurenko *et al.*, 2006; Edgar *et al.*, 2007; Dávila-Harris, 2009) and XRF data from this study. Histogram shows the total number of analyses per SiO_2 bin and schematic trimodal distribution based on the density distribution of samples. (b) Ni (ppm) vs Zr (ppm) bulk-rock; (c) Sr (ppm) vs Zr (ppm) bulk-rock.

low-Sr–low-Ba (Enramada and Gaviotas units) or high-Sr–high-Ba (Adeje and El Abrigo units). Zr and Nb concentrations are positively correlated and range from 300 to 1400 ppm and from 100 to 350 ppm, respectively (Fig. 9b and c).

DISCUSSION

Chemical and textural zoning in ignimbrites

One particularly striking feature of Tenerife ignimbrites visible in the field is their textural variability, manifested as the coexistence of aphyric pumices with crystal-rich pumices (Dávila-Harris, 2009; Dávila-Harris *et al.*, 2013) along with significant amounts of banded pumice. This textural characteristic is commonly associated with gradients in chemistry, degree of welding, temperature and crystallinity throughout the unit (Wolff & Storey, 1984; Wolff, 1985; Bryan, 2006; Dávila-Harris, 2009; Dávila-Harris *et al.*, 2013). Zoning of this type suggests a pre-existing internal stratigraphy within the sampled magma chamber; namely, a relatively aphyric, evolved cap lying atop a more crystal-rich, but hotter portion

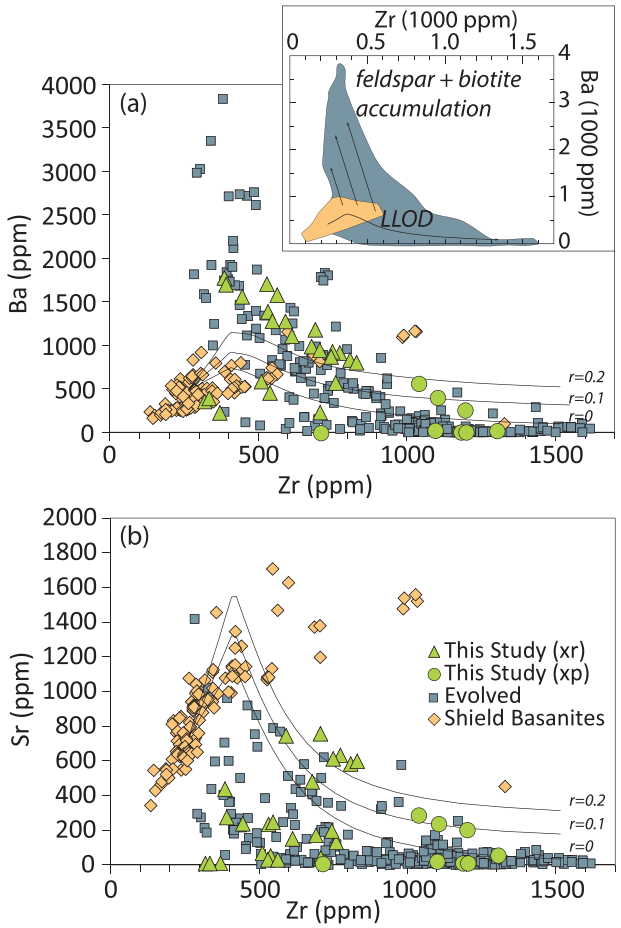

Fig. 5. Bulk-rock Ba vs Zr (a) and Sr vs Zr (b) for the samples from this study, demonstrating: (1) the differences between crystal-poor (xp) and crystal-rich (xr) pumices in terms of Ba content and (2) a clear deviation from the calculated liquid line of descent (LLOD; inset), possibly owing to feldspar accumulation. LLOD calculated with the AFC equation $C_l/C_i = F^{-z} + [r/(r - 1)] \times (C_a/C_o z) \times (1 - F^{-z})$ (DePaolo, 1981) using MELTS phenocryst modal abundances, AN31 basanitic starting composition (0·3% H_2O) and the partition coefficients of Villemant (1988). The hypothetical assimilant (C_a) is a feldspar that contains 5000 ppm Ba, 500 ppm Sr and 0 ppm Zr. The term r represents the ratio of assimilation to crystallization. Literature Tenerife whole-rock data are shown for comparison (Thirlwall *et al.*, 2000; Nichols, 2001; Dávila-Harris, 2009). Inset: schematic deviation toward high Ba and low Zr values is indicative of feldspar and biotite accumulation.

(Wolff *et al.*, 1990; Dávila-Harris *et al.*, 2013; Evans & Bachmann, 2013). The eruption first taps the crystal-poor top and follows by digging into deeper levels of the magma chamber (more crystal-rich). This scheme was laid out by Wörner & Schmincke (1984) and has been observed in many volcanic fields [e.g. it is particularly well documented in the Bishop Tuff (Hildreth, 1979), Crater Lake (Bacon & Druitt, 1988), Ammonia Tanks Tuff (Bachmann & Bergantz, 2008, and references therein; Deering *et al.*, 2011), Peach Spring Tuff (Pamukcu *et al.*, 2013) and Carpenter Ridge Tuff (Bachmann *et al.*, 2014, and references therein)], commonly with some degree of mixing and mingling between different magma horizons (e.g. Hildreth & Wilson, 2007).

Crystal-rich and crystal-poor pumices on Tenerife, although very similar in major element composition (Fig. 4a), differ dramatically in trace element content. The difference between pumices becomes most apparent when comparing Ba, Sr, Eu and Zr contents and is particularly striking in some banded and mafic pumices (Nichols, 2001). Zr is essentially incompatible in alkaline magmas (no zircon crystallization) and is here used as an index of differentiation. In contrast, Ba and Sr increase in the melt in the mafic endmembers until the point of alkali feldspar or plagioclase saturation, after which their concentrations decrease dramatically (liquid line of descent demonstrated in Fig. 5). A careful examination of the Zr vs Ba trend reveals that many low-Zr (presumably less evolved) crystal-rich, banded and 'mafic' pumices contain Ba concentrations (>3000 ppm) in excess of what is possible by following the liquid line of descent (Ablay *et al.*, 1998). More strikingly, these pumices follow a trajectory away from a fractionation trend (i.e. Zr below 500 ppm despite the high Ba). It is unlikely that this trace element signature is due to mixing with tephriphonolite magma, as even the most fractionated magmas contain less than 2000 ppm Ba and have a high Zr content (~800 ppm; see Bryan *et al.*, 2002), which is inconsistent with the banded, crystal-rich pumice chemistry (Fig. 5; Nichols, 2001). Assimilation of sediments (Hoernle, 1998), material from the volcanic edifice (Thirlwall *et al.*, 2000) or nepheline syenite (Wiesmaier *et al.*, 2012) would also be unlikely to produce the trends in Ba owing to the low Ba concentration of each of these reservoirs.

The most likely explanation is that these Ba-rich, crystal-rich, banded and less evolved pumices represent remobilized cumulates rich in alkali feldspar and/or biotite, as these phases strongly partition Ba but not Zr. REE patterns (Fig. 6) are consistent with such an interpretation, with crystal-rich pumices demonstrating a positive Eu anomaly indicative of feldspar accumulation, whereas crystal-poor pumices show a negative anomaly indicative of feldspar fractionation. The crystal-rich clasts are therefore interpreted as portions of a remobilized feldspar-dominated cumulate, an interpretation supported by Ablay *et al.* (1998) for some Ba-rich volcanic rocks reported in their study. Crystal-poor clasts, on the other hand, characterized by low Ba and high Zr (Fig. 5), can be interpreted primarily as highly fractionated residual melts from which feldspar and biotite have been removed.

If crystal-rich pumices do contain partially remobilized cumulates, then we should expect that petrographic textures will reflect this. Indeed, crystal-rich pumices with 20–50% phenocrysts often exhibit intergrown mineral textures or isolated glomerocrysts (Fig. 2), suggesting restricted growth in a high-crystallinity environment. Frequent severe resorption and embayed textures in feldspar indicate strong mineral–melt disequilibrium prior to eruption, and mingling between

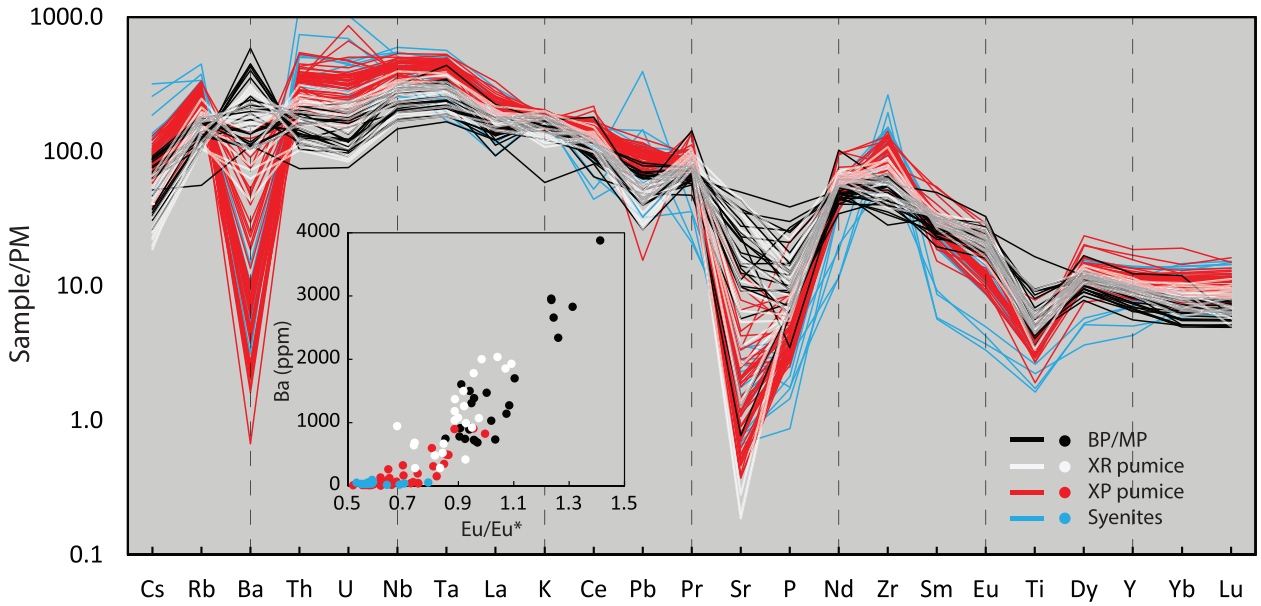

Fig. 6. (a) Bulk-rock trace element patterns of crystal-rich (xr; white; this study), and crystal-poor (xp; red; Nichols, 2001; this study) phonolites, syenites (blue; Nichols, 2001), and banded pumices and mafic pumices (BP and MP; black; Nichols, 2001 and this study) normalized to primitive mantle (PM), following McDonough & Sun (1995). Depletions in Ba and enrichment in Zr in xp units relative to xr and BP/MP units should be noted. Inset: positive correlation of Ba vs Eu anomaly [$Eu^* = \sqrt{(Sm \times Gd)}$]. The low Eu/Eu* in xp samples and syenites should be noted.

phonolitic glass and a more mafic component in the phonolitic samples suggests that a recharge event may have been responsible for this disequilibrium. The presence of mingled pumices in many units (e.g. El Abrigo; Arico) has previously been cited as evidence for mafic magma injection and mixing in the chamber immediately prior to eruption (Wolff, 1985; Araña *et al.*, 1994; Bryan *et al.*, 1998, 2002). Some units show evidence of resorption followed by one or more recrystallization events, indicating periodic thermal fluxing or recharge prior to eruption (Fig. 3a–c).

Remobilization of cumulates may take place by partial melting, mechanical disaggregation or a combination of the two processes following recharge (Wörner & Wright, 1984; Burgisser & Bergantz, 2011; Huber *et al.*, 2011). The latter process can be seen most clearly among the eruptive products of the Gaviotas unit, where preservation of crystal aggregates (anorthoclase + biotite + augite + Fe–Ti oxides + apatite ± titanite ± amphibole) appears the highest, along with high Zr contents (>1000 ppm; Fig. 9) and low Ba and Sr contents (<300 and <50 ppm, respectively) in glass, together suggesting that these samples represent a cumulate horizon that was mobilized wholesale together with its interstitial liquid without significant melting. Thermal remobilization and partial melting, on the other hand, is most evident in the Arico unit, where aggregate preservation is low, and feldspar trace element chemistry necessitates the creation of an 'enriched' melt, as outlined below.

Compositional zoning in feldspar and biotite preserves a record of the melt composition from which the mineral crystallized. Zoned feldspar crystals show minor reverse zoning in An content and extremely Ba-rich rims with concentrations of up to ~15 000 ppm. This necessitates a Ba host liquid concentration of ~1500 ppm, using a liberal estimate of 10 for $K_{Ba}^{fsp-melt}$ (Nash & Crecraft, 1985). If intermediate magmas on Tenerife (using phonotephritic rift lavas as a proxy) are assumed to provide the recharge, it follows that the feldspars in question cannot be crystallizing directly from this melt (which has on average ~500 ppm Ba), but must instead crystallize from pockets of melt locally enriched in Ba. Rare tephriphonolites have higher Ba contents and could be the source of the high-Ba minerals (Bryan *et al.*, 2002). However, the Sr content of these melts (~500–1000 ppm) would crystallize feldspar with 2500–5000 ppm Sr, assuming a K_D of five (Wörner *et al.*, 1983; Nash & Crecraft, 1985; Villemant, 1988). As Sr content in feldspars is typically <1000 ppm, and in some cases <400 ppm (Arico; Fig. 7c), this interpretation is precluded. Moreover, those tephriphonolites are some of the rarest magmas on Tenerife (Fig. 4a).

Zoned biotites also show clear patterns of growth and regrowth from melts with variable Ba and Rb concentrations (Figs 3d–f and 8). All units contain biotite phenocrysts with Ba-enriched rims, most notably the Arico and El Abrigo units, where Ba concentration typically exceeds 20 000 ppm and occasionally approaches 35 000 ppm. Assuming a generous K_D of 20 (Villemant, 1988), the concentration of Ba in the melt would need to be 1000–1500 ppm, which, as previously noted, is extremely high for most intermediate magmas in Tenerife. Furthermore, the negative correlation of Rb and Ba speak against crystallization directly from a recharge melt (Fig. 8c). Because Rb and Ba are both

Table 3: Representative feldspar, biotite and glass compositions

	Feldspar								Glass				
Unit:	Enramada	Gaviotas	Arico		Adeje		El Abrigo		Enramada	Gaviotas	Arico	Adeje	El Abrigo
Sample:	007	019	031 (rim)	031 (core)	015 (rim)	015 (core)	043 (rim)	043 (core)	007	019	031	015	043
SiO_2	65·96	62·57	65·15	66·61	64·52	66·17	62·13	62·06	60·66	58·03	59·52	59·80	56·62
TiO_2	0·09	0·10	0·15	0·10	0·11	0·11	0·13	0·12	0·84	0·97	0·88	0·95	0·87
Al_2O_3	19·63	21·92	20·23	19·45	20·75	19·83	22·34	22·57	16·88	18·30	17·52	16·99	19·53
FeO	0·36	0·33	0·34	0·37	0·38	0·38	0·37	0·33	2·71	2·85	3·02	3·21	3·31
MgO	0·00	0·00	0·00	0·00	0·01	0·00	0·01	0·00	0·62	0·54	0·66	0·77	0·60
CaO	0·93	3·19	1·09	0·68	1·68	0·90	3·15	4·03	0·69	0·88	0·90	0·95	2·19
Na_2O	7·89	8·16	8·53	8·64	8·76	8·85	7·26	7·51	7·59	7·91	8·46	8·15	8·33
K_2O	4·60	2·07	3·21	3·76	2·59	3·28	2·90	2·28	5·25	6·21	4·75	4·35	4·89
SrO	0·00	0·14	0·00	0·01	0·09	0·03	0·26	0·11	0·00	0·00	0·00	0·00	0·08
BaO	0·20	0·39	1·11	0·20	0·89	0·33	1·59	0·80	0·05	0·06	0·31	0·13	0·13
Total	99·66	98·87	99·81	99·83	99·78	99·88	100·14	99·81	95·30	95·74	96·02	95·30	96·54
An	0·04	0·16	0·05	0·03	0·08	0·04	0·16	0·20					
Or	0·27	0·12	0·19	0·22	0·15	0·19	0·18	0·13					
Ab	0·69	0·72	0·76	0·75	0·77	0·77	0·67	0·67					

	Biotite											
Unit:	Enramada	Gaviotas	Arico		Adeje		El Abrigo		Arico (Fig. 3)*			
Sample:	001	019	031 (rim)	031 (core)	010 (rim)	010 (core)	043 (rim)	043 (core)	031_5r	031_5c	031_8r	031_8c
SiO_2	38·25	37·28	36·00	38·04	37·32	37·80	35·67	37·31	36·56	38·37	35·50	36·5
TiO_2	7·30	6·43	8·06	6·35	6·95	6·83	7·12	6·96	7·75	6·26	8·56	7·96
Al_2O_3	12·84	13·05	13·49	12·95	12·74	12·71	13·95	13·73	13·50	12·89	13·67	13·53
FeO	11·22	13·00	11·34	10·58	10·74	10·74	14·49	13·43	11·06	10·97	11·22	10·94
MgO	16·51	15·26	15·58	17·11	16·88	16·70	13·54	14·39	15·69	17·39	14·92	15·62
MnO	0·35	0·45	0·37	0·40	0·39	0·35	0·38	0·39	0·38	0·34	0·40	0·34
CaO	0·00	0·00	0·01	0·00	0·02	0·00	0·01	0·00	0·00	0·00	0·00	0·00
Na_2O	1·17	0·98	1·30	1·32	1·44	1·28	0·91	0·90	1·32	1·25	1·25	1·34
K_2O	8·75	9·02	7·48	8·27	8·17	8·29	8·59	9·05	7·80	8·54	7·19	7·58
Cr_2O_3	0·04	0·02	0·00	0·01	0·01	0·00	0·00	0·00	0·00	0·00	0·04	0·00
Sr (ppm)	0·7	14·5	6·8	0·6	16·2	10·3	36·5	5·7	5·7	0·6	14·2	7·7
Ba (ppm)	917	3120	20307	2413	8048	4714	15513	1739	19838	1138	34541	22307
Rb (ppm)	139	302	146	225	149	166	201	248	153	255	128	148
Total†	96·42	95·89	93·62	95·03	94·65	94·70	94·66	96·16	94·06	96·01	92·75	93·81
Mg#	72·4	67·7	71·0	74·2	73·7	73·5	62·5	65·6	71·7	73·9	70·3	71·8

*Compositions of biotites shown in Fig. 3.
†Totals do not include trace elements.
c, core, r, rim; all oxides wt % unless otherwise noted.

incompatible in less evolved melts, the two elements would form a positive correlation in biotite if the biotite was crystallizing directly from a primitive melt before feldspar saturation. However, the low Rb associated with high Ba concentration is consistent with a parent melt that has been doped with a high-Ba, low-Rb melt. The generation of such extreme mineral compositions involves high-Ba feldspar and biotite crystallizing from pockets of partially melted alkali feldspar cumulate or crystal mush following recharge [see Ammonia Tanks (Deering *et al.*, 2011) and Carpenter Ridge Tuff (Bachmann *et al.*, 2014) studies for similar characteristics].

High Ba rims on feldspar have been noted previously (e.g. Bryan *et al.*, 2002) and paired with observations of high FeO, TiO_2, and/or An content (Triebold *et al.*, 2006; Andújar *et al.*, 2013). These effects were attributed to a shift in melt temperature and composition by addition of a hotter mafic recharge. Here we focus on the Ba zonation in particular, and explicitly assert that this phenomenon is possible only through crystallization from a melt that has been altered by the addition of feldspar partial melt during remobilization of cumulates. This model is, however, consistent with the involvement of mafic recharge, as the melting of a feldspar cumulate requires addition of heat and/or H_2O, both obtainable by recharge [see Wolff *et al.* (2015) for additional details on the process].

Compositional gaps in the Tenerife volcanic series

The number of samples for a given composition varies considerably in Tenerife, leading to the presence of compositional peaks and gaps, a feature that was first noticed decades ago (Fig. 4; Chayes, 1963; e.g. Ridley,

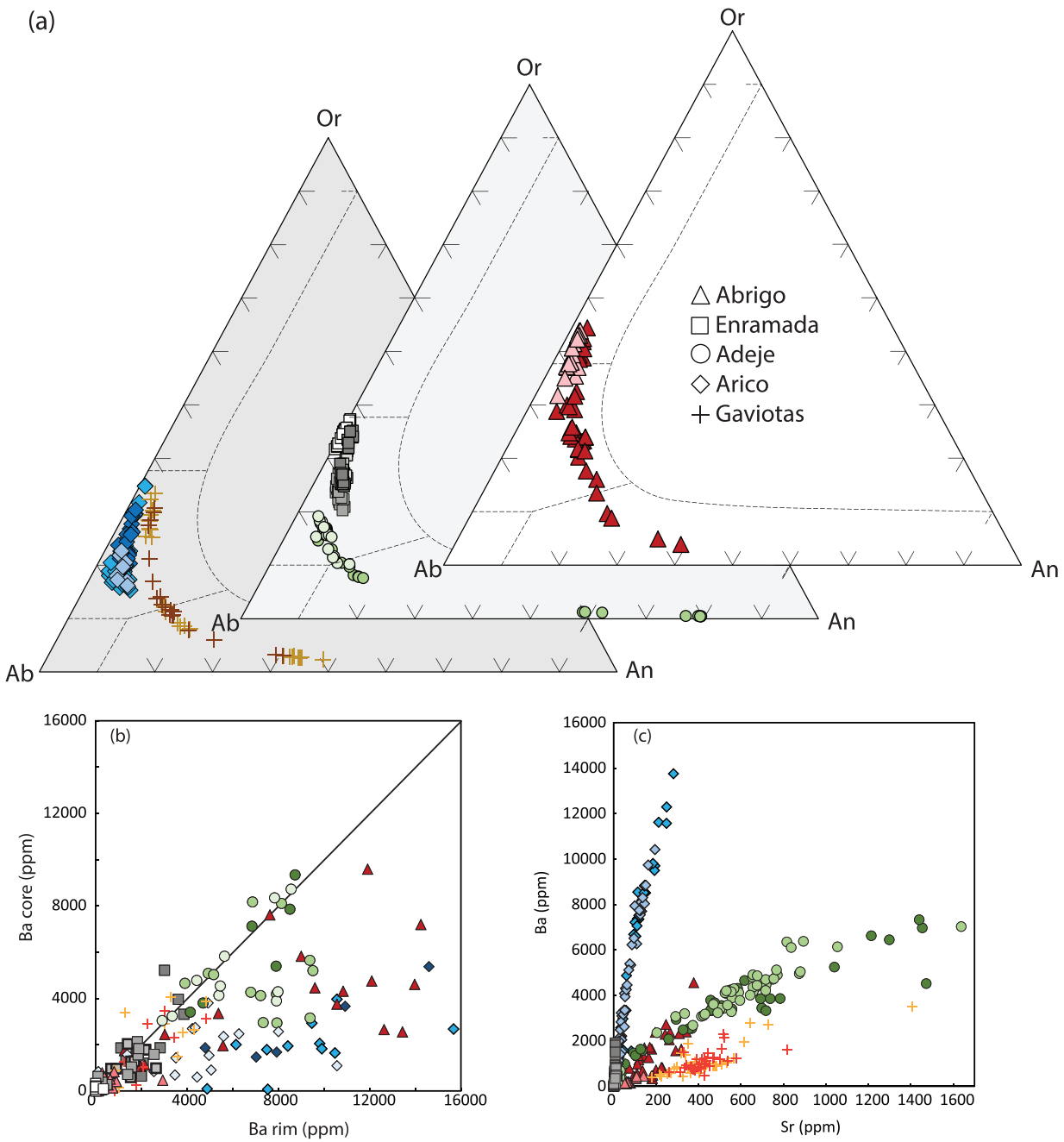

Fig. 7. (a) Feldspar endmember compositions, calculated as molar proportions of Ca, Na or K to (Ca + Na + K), denoted An, Ab and Or, respectively. (b) Ba rim vs core compositions (EPMA; thin section), indicating zonation in the Adeje, El Abrigo and Arico units. Different colors of symbols represent different samples within the same unit: El Abrigo (TFE_12_043, 045), Enramada (TFE_12_001, 005, 007, 065), Adeje (TFE_12_009, 010, 015), Arico (TFE_12_029, 030, 031) and Gaviotas (TFE_12_019, 020). (c) Ba (ppm) vs Sr (ppm) by LA-ICP-MS (grain mount) showing concurrent high Ba with low Sr in the Arico unit. The the slight mismatch in Ba concentrations in (b) and (c) is the result of different analytical techniques and samples.

1970; Wolff & Storey, 1984; Bryan *et al.*, 2002; Wiesmaier *et al.*, 2012). As previous studies have strongly suggested that magmatic differentiation is dominated by fractionation from mafic parents (Wolff & Palacz, 1989; Ablay *et al.*, 1998; Neumann *et al.*, 1999; Bryan *et al.*, 2002), such gaps can be explained by crystal–melt separation from crystal mushes at intermediate crystallinities (mechanical control on phase separation; Dufek & Bachmann, 2010). We have tested this hypothesis for Tenerife magmas, and use thermodynamic modeling (rhyolite-MELTS) to try to reproduce the observed compositional gaps on Tenerife.

Whole-rock data from Tenerife (using compiled data from the GEOROC database) demonstrate a clear trimodality in chemical composition, suggesting that magmatic processes preferentially release distinct compositions (Fig. 4a). A histogram paired with a TAS diagram (Le Bas *et al.*, 1986) allows identification of (1)

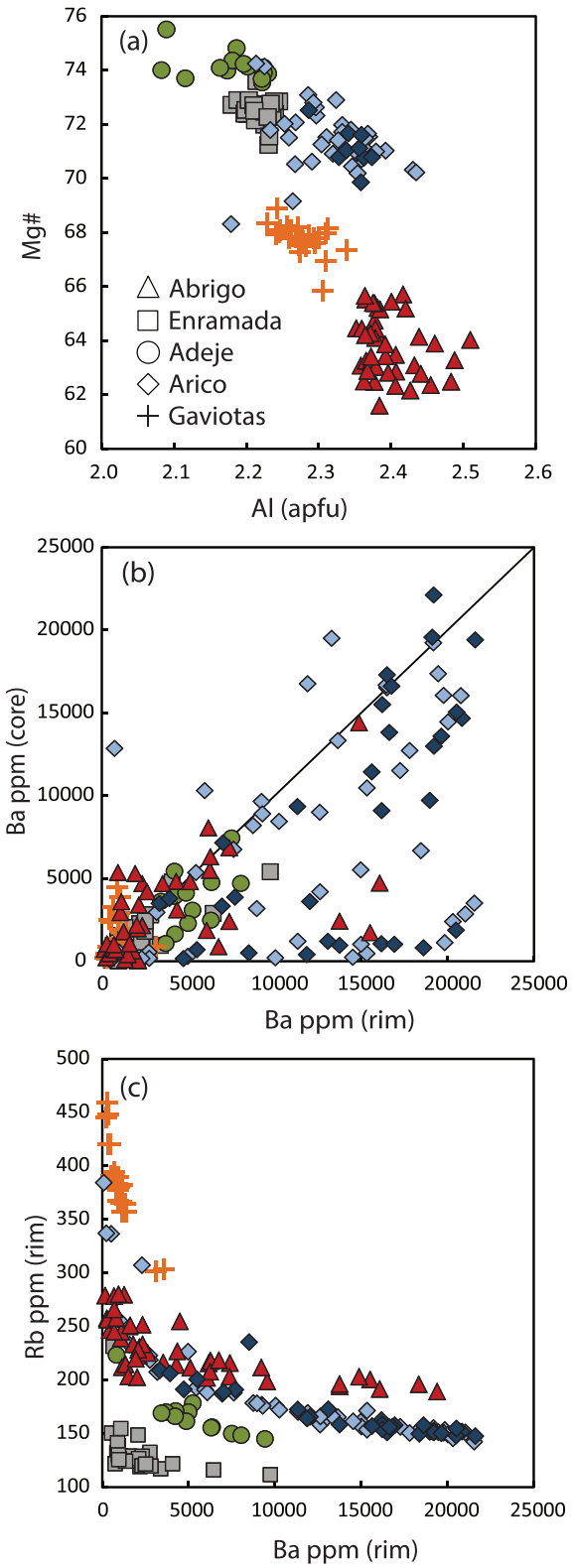

Fig. 8. (a) Tenerife biotite major element compositions: aluminum atoms per formula unit (a.p.f.u.) vs Mg# [Mg/(Mg + Fe)]; (b) Ba zonation in rim vs core, showing particularly intense zonation in the Arico unit; (c) Ba vs Rb. Relative error on laser measurements is ~5%. Different colors of symbols represent different samples within the same unit: El Abrigo (TFE_12_043), Enramada (TFE_12_001), Adeje (TFE_12_010), Arico (TFE_12_029, 031) and Gaviotas (TFE_12_019).

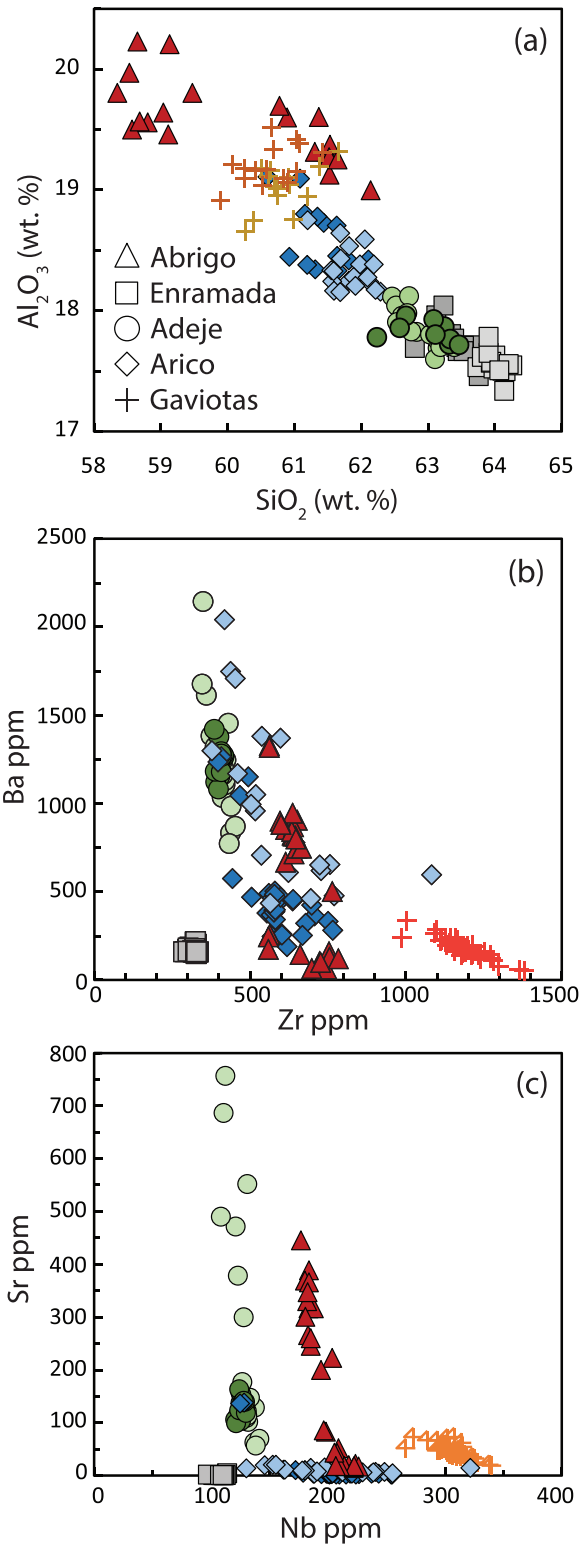

Fig. 9. Glass major and trace element compositions from all studied units: (a) SiO_2 vs Al_2O_3 (wt %) normalized to 100%; (b): Ba vs Zr; (c) Sr vs Nb (ppm). Different colors of symbols represent different samples within the same unit: El Abrigo (TFE_12_043), Enramada (TFE_12_001, 007), Adeje (TFE_12_010, 015), Arico (TFE_12_030, 031) and Gaviotas (TFE_12_019, 020).

basanitic, (2) phonotephritic and (3) phonolitic compositions (*sensu lato*). Comparison of these three groups in terms of trace element content reveals a sharp drop in Ni content from basanite to phonotephrite, and a drop in Sr content from phonotephrite to phonolite (Fig. 4b and c). These observations suggest the fractionation of large amounts of olivine or pyroxene from the basanites and plagioclase from the phonotephrites to form the phonotephrites and phonolites, respectively. It should be noted that whereas intermediate lavas are often visibly mingled, the data plotted here lie along a fractionation trend, which for the most part is inconsistent with an origin purely by magma mixing (Fig. 4b and c). Apart from the fact that mixing between contrasting magmatic compositions in extremely difficult to achieve (e.g. Sparks & Marshall, 1986), blending between typically high-Ni–low-Sr basanite and low-Ni–low-Sr phonolites would not lead to the low-Ni–high-Sr phonotephrites (Fig. 4b and c). Mixing between more evolved compositions (phonotephrites and phonolites) can occur, but this process obviously cannot produce the phonotephritic magma itself (see similar arguments made for volcanic series in different tectonic settings; e.g. Wade *et al.*, 2005; Lee & Bachmann, 2014; Mancini *et al.*, 2015; Szymanowski *et al.*, 2015).

Optimal melt extraction from a crystal mush should take place at intermediate crystallinity, controlled by the onset of rheological lock-up (i.e. convection no longer possible) and enhanced by thermal buffering from the latent heat of crystallization (Dufek & Bachmann, 2010). Low-crystallinity systems experience enhanced convective stirring and heat loss (Marsh, 1981; Koyaguchi & Kaneko, 1999), which precludes efficient melt–solid segregation owing to rapid crystallization (i.e. short lifetime) and constant re-entrainment of crystals into convective cells (Burgisser *et al.*, 2005; Huber *et al.*, 2009). At high crystallinities, melt permeability reaches very low values within the crystal mush, again leading to inefficient melt extraction. Therefore, intermediate-crystallinity magmas are those from which melt is most efficiently extracted. It is possible, using thermodynamic MELTS simulations, to predict the melt major element composition of a magma within these constraints, assuming a known starting composition. It should be noted that although MELTS is not optimized for alkaline compositions, it has been used successfully in such provinces in the past (e.g. Bohrson *et al.*, 2006; Fowler *et al.*, 2007; Rooney *et al.*, 2012). These paired thermochemical and thermomechanical simulations can therefore provide a model for the generation of Tenerife's compositional gaps and chemical diversity.

A two-stage fractionation model is considered, whereby a deep basanitic magma reservoir generates relatively discrete phonotephritic melts at intermediate crystallinity, which upon extraction are emplaced in a shallower magma reservoir and generate phonolitic melts via the same mechanism. This two-stage model is based on suggestions of polybaric differentiation by previous researchers (Ablay *et al.*, 1998; Freundt-Malecha *et al.*, 2001; Klügel *et al.*, 2005). It is also supported by mineral associations within the crystal-rich pumices. Slightly resorbed mafic phases (augite + Fe–Ti oxides + apatite ± titanite ± biotite ± amphibole ± sulfides) form minute glomerocrysts (<1 mm) and can commonly be found within darker, less evolved bands, suggesting that the recharge contains parts of a remobilized mafic mush. Meanwhile, anorthoclase forms glomerocrysts of up to 10 mm (commonly together with biotite and/or haüyne); this finding indicates accumulation of feldspars and associated low-*P*, low-*T* phases at shallower levels in the crust [see Ellis *et al.* (2014) for similar characteristics]. Taken together, these two glomerocryst types are consistent with the presence of at least two major magma reservoirs at different depths beneath Tenerife, as indicated by previous studies (Ablay *et al.*, 1998; Neumann *et al.*, 1999; Klügel *et al.*, 2005). The eruption of the residual melts in the two reservoirs at these favorable levels of differentiation (in addition to the eruption of parental basanite prior to fractionation) would over time generate the observed trimodal chemical distribution on Tenerife. The crystal-rich and crystal-poor phonolites discussed above are a tertiary stage in the evolution, operating on the same principles but no longer able to generate large differences in major element chemistry.

Table 4: MELTS model parameters

Designation	Basanite (AN31)	Phonotephrite average* ($n = 105$)
Composition (wt %)		
SiO_2	42·83	48·34
TiO_2	4·08	2·86
Al_2O_3	13·99	17·47
FeO_T	12·86	9·15
MnO	0·22	0·20
MgO	6·90	4·32
CaO	11·71	8·03
Na_2O	3·40	4·98
K_2O	1·01	2·29
P_2O_5	1·05	1·01
H_2O	0·3/1·0	1·5/2·5/3·5
Intensive parameters		
Liquidus T (°C)	1231/1219	1153/1148/1148
P (bar)	4000	1500
Mode	NF	NF
fO_2 buffer	NNO†	QFM†

NF, no fractionation.
*Phonotephrites are from GEOROC database and are defined as containing between 46 and 54 wt % SiO_2 and between 6 and 8 wt % $Na_2O + K_2O$.
†Oxygen buffer set to find liquidus, then removed during simulation.

MELTS simulations—magma reservoir processes

Model parameters for the MELTS simulations are summarized in Table 4 and described in detail below.

Pressure

Although several studies indicate pyroxene crystallization at mantle pressures (6–9 kbar; see Ablay *et al.*,

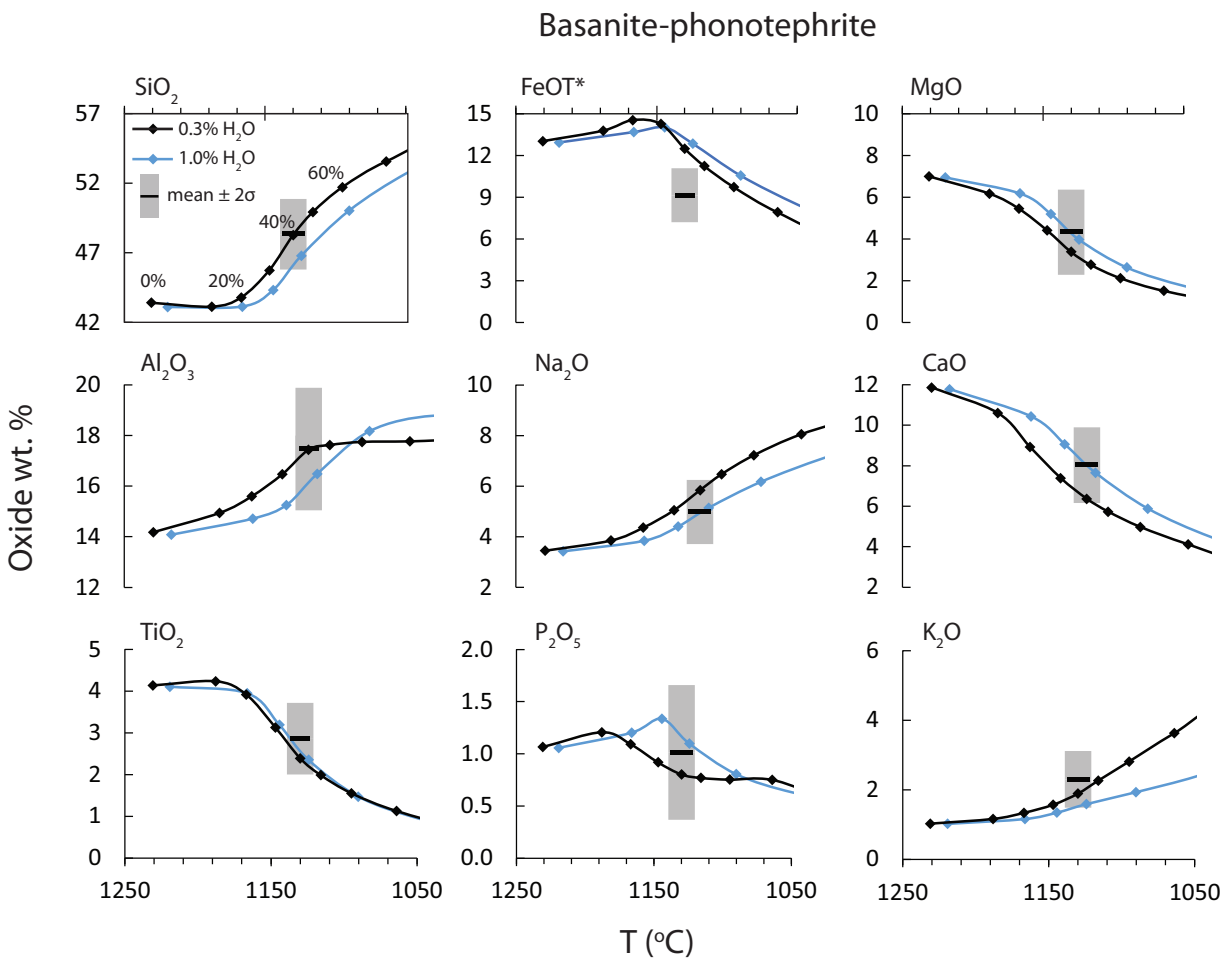

Fig. 10. MELTS simulations of basanite to phonotephrite evolution (Table 4) showing major oxides (wt %) vs temperature (°C). Starting composition AN31 (Thirlwall *et al.*, 2000). Black lines represent 0·3% H_2O in the starting composition; blue lines represent 1·0%. Grey bars show average phonotephritic compositions from the literature with 2σ error. Tick marks show the total crystallinity of the system at each stage of the simulation.

1998; Neumann *et al.*, 1999), there is also evidence of major magma stagnation and underplating at the base of the crust, at ~4 kbar (Klügel *et al.*, 2005). We therefore use this pressure for the basanite fractionation stage. For a shallow reservoir, we select a pressure of 1·5 kbar, following pressure estimates and phase equilibrium experiments by Ablay *et al.* (1995) and Andújar *et al.* (2008), respectively.

Oxygen fugacity

Following fO_2 determinations from Fe–Ti oxides by Ablay *et al.* (1998), we set the liquidus oxygen fugacity at the nickel–nickel oxide buffer (NNO) for the basanite–phonotephrite stage and at the quartz–fayalite–magnetite buffer (QFM) for the phonotephrite–phonolite stage, respectively. After calculating the liquidus, the buffer is removed and the system is allowed to equilibrate at lower temperatures.

Starting composition

An aphyric basanitic lava (AN31; Thirlwall *et al.*, 2000) is selected as the starting composition for this model, as it represents a typical basanitic composition relatively devoid of crystals and therefore approximately represents a liquid composition. An average of 105 phonotephritic lavas (in the range of 46–54 wt % SiO_2 and 6–8 wt % $Na_2O + K_2O$) is selected as the starting composition for the second stage.

Water content

For the basanite, initial H_2O concentrations of 0·3% and 1% are selected, representing a dry and a wet basanite. For the phonotephrite, 1·5%, 2·5% and 3·5% H_2O are selected, corresponding to the fractionated melts from the dry and wet runs in the first stage.

Latent heat of crystallization

The latent heat of the system is calculated from MELTS output by subtracting the sensible heat change (calculated as the product of temperature step and the average heat capacity per step) from the change in total enthalpy of the system. The ratio of the latent heat of the system to the sensible heat is a proxy for the crystallization of a new phase, and if the ratio is greater than

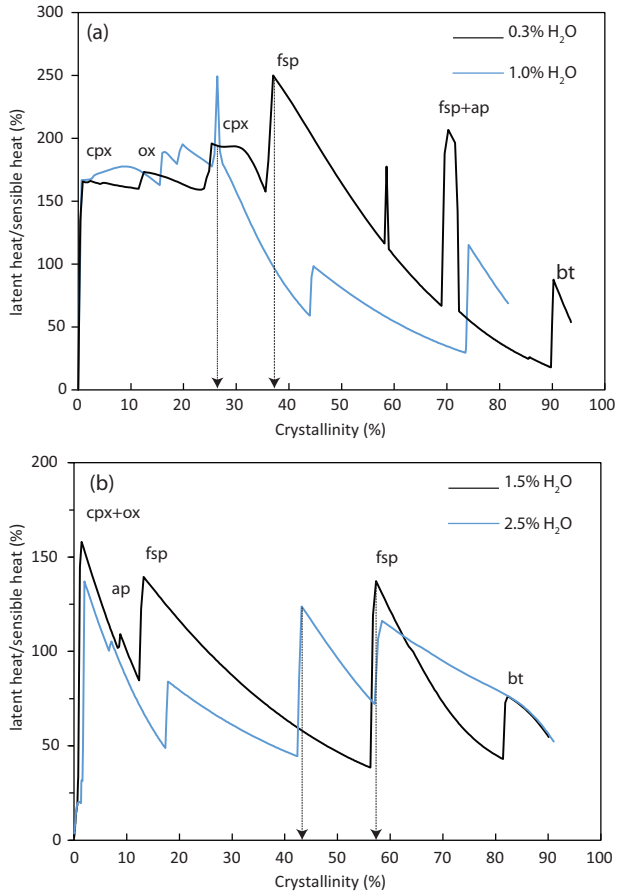

Fig. 11. Latent heat vs crystallinity profiles for (a) basanite to phonotephrite and (b) phonotephrite to phonolite evolution, each with variable H_2O content. Latent heat divided by sensible heat is plotted on the *y*-axis, demonstrating distinct peaks where the enthalpy of the system is controlled by crystallization and the system is thermally buffered. Crystallizing phases are labelled at each peak: fsp, feldspar; cpx, clinopyroxene; ox, Fe–Ti oxides; ap, apatite; bt, biotite.

unity, the system's enthalpy loss is predominantly manifested as mineral crystallization (Morse, 2011). Spikes in latent heat or sensible heat coincide with the crystallization of new phase, and at these moments, the sensible heat loss of the system is diminished (assuming a constant Joule flux out of the system). This results in a system being thermally 'buffered', whereby crystallization slows down, providing more time for crystal–melt separation. Assuming little to no convection (probably at >30% crystals), these latent heat spikes help maintain the magmas at a given crystallinity for longer periods of time, enhancing melt extraction.

Results

Model oxide concentrations fit literature data well for the basanite to phonotephrite evolution, with best fit (determined by least-squares minimization) at ~35% and ~45% crystallinity for the wet and dry basanites (Fig. 10), respectively. This coincides with latent heat spikes at ~26% and ~37% crystallinity (Fig. 11a). Likewise, model data from the phonotephrite–phonolite model adequately fit literature data, with best fit occurring at ~47% and ~57% crystallinity for the wet and dry phonotephrites (Fig. 12), corresponding to latent heat spikes at ~45% and ~58% (Fig. 11b). Systematic offsets between the model and literature values are stronger in the second stage. It is unclear whether these are caused by: (1) shortcomings of the MELTS model in reproducing appropriate compositions for feldspar, which makes up the majority of the mineral assemblage; (2) influence of open-system processes including magma mixing and crustal assimilation; (3) the partial melting of low-temperature phases such as feldspar, which is supported by the existence of the feldspar partial melts documented in this study; or (4) some combination of the above processes.

The most striking feature of the MELTS simulations is the coincidence of latent heat spikes with crystallinities at which the residual melt most closely resembles literature values for phonotephrites and phonolites. In the first stage of the simulations, the spikes occur near crystallinities where convection slows owing to the presence of incipient crystal networks (Davis & Acrivos, 1985; Saar *et al.*, 2001), allowing hindered settling to occur. For phonotephrite–phonolite evolution, the most pronounced latent heat spike occurs within the crystallinity window calculated by Dufek & Bachmann (2010), consistent with the interpretation that melt extraction in this range is preferred in part because of latent heat buffering. These findings are further supported by numerical simulations by Gelman *et al.* (2013), which indicate that incorporation of near-eutectic behavior in cooling sills (i.e. latent heat buffering) enhances the longevity of silicic magma reservoirs.

The phonotephrite–phonolite MELTS model, as noted above, does not re-create average phonolite compositions perfectly, showing depletions in SiO_2, Na_2O and Al_2O_3 of ~2, ~1 and ~2 wt %, respectively, and smaller offsets in other major elements (Fig. 11). This can be due to a number of factors. First, MELTS crystallizes sanidine and plagioclase in lieu of the anorthoclase typical of Tenerife (i.e. lower Al_2O_3 and CaO and higher SiO_2, Na_2O and K_2O than the MELTS feldspar compositions). Crystallizing the actual feldspar composition would, on qualitative evaluation, increase Al_2O_3 and CaO in the melt while decreasing SiO_2, Na_2O and K_2O concentrations, and hence help towards resolving the numerical offset. Second, mixing of the residual melt with recharge melt in natural samples would drive the composition (particularly in FeO, MgO and TiO_2 content) away from the model predictions, and this mixing is not accounted for in the model. Partial assimilation of syenite or basanite (Wiesmaier *et al.*, 2012) may present a plausible mechanism for creating the observed major element compositions, particularly as the major element composition of the syenites closely matches that of phonolites (Wolff *et al.*, 2000). However, partially melting subsolidus material presents thermal challenges, as discussed below.

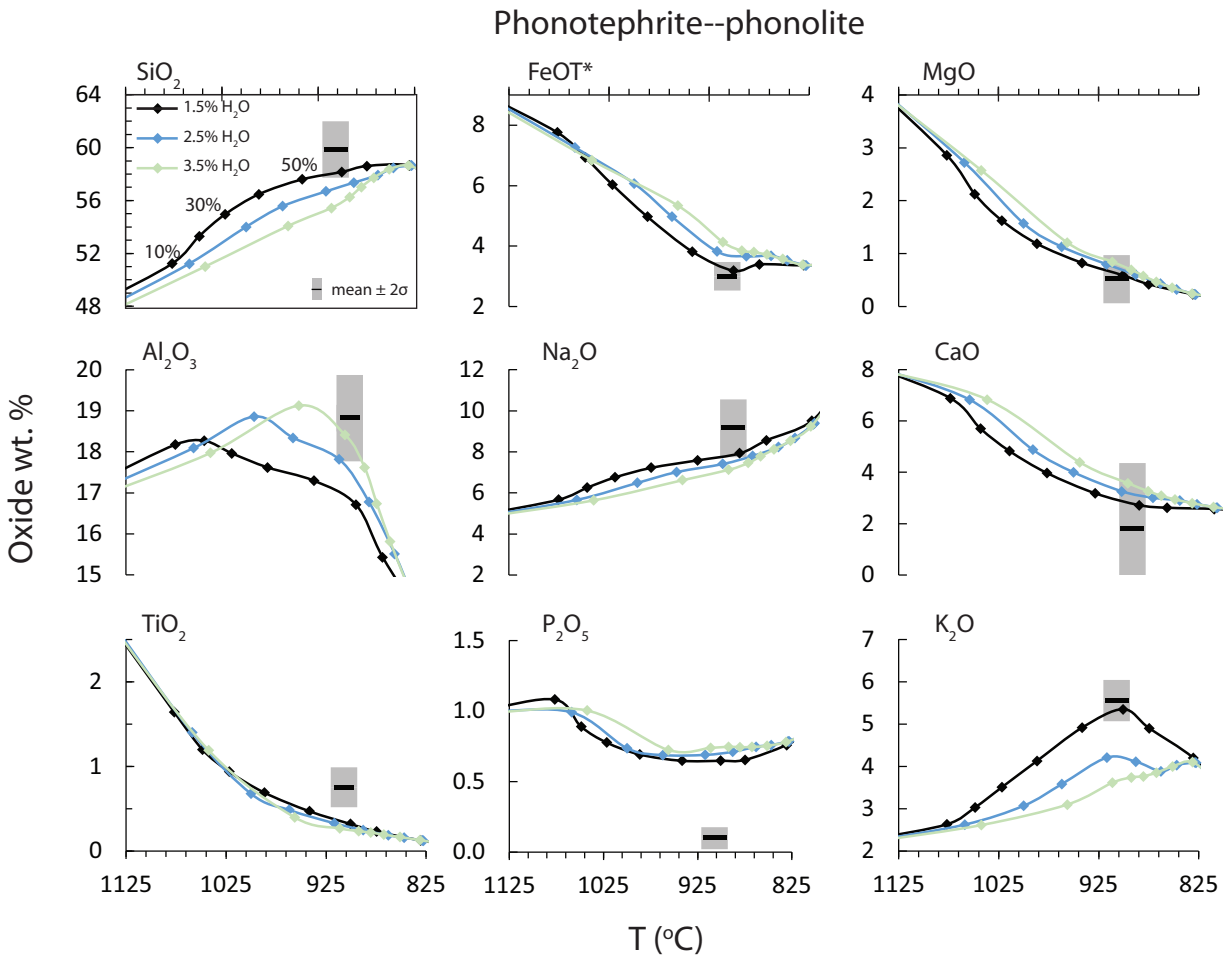

Fig. 12. MELTS simulations of phonotephrite to phonolite evolution (Table 4) showing major oxides (wt %) vs temperature (°C). Starting composition is the average of literature phonotephrites (46–54 wt % SiO_2 and 6–8 wt % $Na_2O + K_2O$). Black, blue and green lines represent 1·5%, 2·5% and 3·5% starting H_2O content, respectively. Grey bars show average phonolitic compositions from the literature with 2σ error. Tick marks show the total crystallinity of the system at each stage of the simulation.

Two considerations must be made when discussing partial melting of the crust surrounding an intrusion or recharge magma: (1) partial melting is enhanced by adding volatiles; (2) advective heat transfer is more efficient than conductive heat transfer. Taken together, this means that the partial melting of a fully solidified and degassed syenitic pluton by mafic underplating is much less energetically favorable than partially melting a volatile-rich crystal mush still containing residual melt (Huber *et al.*, 2011). Advective heating through disaggregation and partial homogenization of an evolved crystal mush by recharge in the latter scenario leads to more efficient heat exchange and allows for the partial melting of low solidus temperature phases (e.g. alkali feldspar), as discussed above. This combination of the residual melt extracted from the crystal mush with some amount of partial remelting of the leftover (but still melt-bearing) cumulate leads to the observed chemical and textural zoning in the ignimbrites. Coincidentally, the addition of cumulate melt (perhaps with some nepheline or haüyne addition) would shift the residual melt composition toward higher Al_2O_3, Na_2O and SiO_2 concentrations, correcting some of the major element inconsistencies between MELTS models and natural rock compositions. This process of feldspar cannibalization, or 'cognate cumulate melting' has been suggested for a number of silicic ignimbrites [see review by Wolff *et al.* (2015)] and for deeper levels in the magmatic system on Tenerife ('AFC with authigenic cumulate rocks'; see Wiesmaier *et al.*, 2013). We assert that this effect is probably as pronounced in the upper crust, and is also consistent with trace element chemistry (in minerals and bulk-rocks) as discussed above.

The polybaric differentiation model described here (building on the work of previous researchers in the Canary Islands and elsewhere; e.g. Lipman *et al.*, 1978; Ablay *et al.*, 1998; Freundt-Malecha *et al.*, 2001; Klügel *et al.*, 2005) is favored for a number of reasons: (1) assuming that MELTS results are accurate to a first order, we reproduce the trimodality in Tenerife melt compositions; (2) Ba- and Eu-rich, but Zr-, Rb- and Sr-poor crystal-rich pumices, with Ba-rich rims on alkali feldspar and biotite, indicate the presence of an unusual melt, obtainable by partially melting an alkali

feldspar-rich cumulate; (3) strong Ba depletion in crystal-poor pumices is consistent with them being the extracted residual melts from a feldspar accumulation zone; (4) frequent, small-volume eruptions throughout the eruptive history of Teide serve as a rough proxy for mafic–intermediate recharge into the phonolitic magma chamber, making near-continuous rejuvenation and cumulate melting possible; mass addition from these recharges (Bryan *et al.*, 2002) may cause additional complexities in the trace element signatures; finally, (5) thermal models (Gelman *et al.*, 2013; Karakas & Dufek, 2015) and geochronological studies (Reid *et al.*, 1997; Brown & Fletcher, 1999; Schmitt *et al.*, 2003; Charlier *et al.*, 2005; Bachmann *et al.*, 2007; Costa, 2008; Simon *et al.*, 2008) suggest that upper crustal silicic mushes have extended lifetimes, making crystal–melt extraction feasible.

CONCLUSIONS

The major findings of this study are as follows.

1. Some evolved magmas below Tenerife exist in a mushy state characterized by highly crystalline, interlocked textures. Periodic recharge creates thermal and chemical disequilibrium (strong resorption and embayments) in low-temperature phases (e.g. anorthoclase and biotite phenocrysts), generating a Ba-enriched, Zr-poor interstitial melt, part of which then recrystallizes as Ba-enriched rims in feldspar and biotite. The accumulation of Ba-rich feldspar–biotite horizons within the crystal mush generates a bulk composition that is high-Ba and low-Zr following melt extraction, plotting on a trend that is away from the liquid line of descent. Explosive phonolitic eruptions may sample both the extracted residual (± cumulate) melt (crystal-poor pumice) and its associated mushy cumulate (crystal-rich pumice), generating zoned deposits with a range in pumice textures.
2. MELTS models indicate that the melt extracted from a crystallizing basanitic system at ~40 vol. % crystallinity is roughly consistent with intermediate lava compositions on Tenerife (phonotephritic). Using phonotephritic lavas as starting compositions and separating melt at 60 vol. % crystals (representing the extraction of phonolitic melt from a crystal mush at shallow depth) approximately reproduces the chemical compositions of the Tenerife phonolites. Preferential melt extraction enhanced by latent heat buffering at intermediate crystallinities in lower and upper crustal magma reservoirs may generate a volcanic record with a trimodal distribution, providing a plausible mechanism for the generation of the Bunsen–Daly Gap in Tenerife and other volcanic and plutonic provinces where crystal fractionation dominates magma differentiation. However, open-system processes, particularly auto-assimilation of cogenetic, fusible, silicic cumulates, mixing between different magma batches, and various degrees of crustal assimilation also play a vital role in generating the complex geochemical signatures that are observed on Tenerife and in other magmatic provinces.

ACKNOWLEDGEMENTS

This study has benefited greatly from the help of many people. We acknowledge Marcel Guillong, Lukas Martin and Juliana Troch and the University of Kiel microprobe facility for laboratory assistance. We thank Mark Ghiorso, John Wolff and Lauren Cooper for their thoughtful comments on earlier versions of the paper, and acknowledge constructive reviews by Gail Mahood, Patricia Larrea, Scott Bryan and an anonymous reviewer. Finally, we thank Gerhard Wörner for editorial handling, discussion and providing many insightful comments in the finalizing of the paper.

FUNDING

This project was supported by Swiss National Science Foundation grant 200021_146268.

SUPPLEMENTARY DATA

Supplementary data for this paper are available at *Journal of Petrology* online.

REFERENCES

Abdel-Monem, A., Watkins, N. & Gast, P. (1971). Potassium–argon ages, volcanic stratigraphy, and geomagnetic polarity history of the Canary Islands; Lanzarote, Fuerteventura, Gran Canaria, and La Gomera. *American Journal of Science* **271**, 490–521.

Ablay, G., Ernst, G., Marti, J. & Sparks, R. (1995). The ~2 ka subplinian eruption of Montaña Blanca, Tenerife. *Bulletin of Volcanology* **57**, 337–355.

Ablay, G., Carroll, M., Palmer, M., Martí, J. & Sparks, R. (1998). Basanite–phonolite lineages of the Teide–Pico Viejo volcanic complex, Tenerife, Canary Islands. *Journal of Petrology* **39**, 905–936.

Ancochea, E., Huertas, M., Cantagrel, J., Coello, J., Fúster, J., Arnaud, N. & Ibarrola, E. (1999). Evolution of the Cañadas edifice and its implications for the origin of the Cañadas Caldera (Tenerife, Canary Islands). *Journal of Volcanology and Geothermal Research* **88**, 177–199.

Andújar, J., Costa, F., Martí, J., Wolff, J. & Carroll, M. (2008). Experimental constraints on pre-eruptive conditions of phonolitic magma from the caldera-forming El Abrigo eruption, Tenerife (Canary Islands). *Chemical Geology* **257**, 173–191.

Andújar, J., Costa, F. & Scaillet, B. (2013). Storage conditions and eruptive dynamics of central versus flank eruptions in volcanic islands: the case of Tenerife (Canary Islands, Spain). *Journal of Volcanology and Geothermal Research* **206**, 62–79.

Araña, V. & Brändle, J. (1969). Variation trends in the alkaline salic rocks of Tenerife. *Bulletin Volcanologique* **33**, 1145–1165.

Araña, V., Martí, J., Aparicio, A., García-Cacho, L. & García-García, R. (1994). Magma mixing in alkaline magmas: An example from Tenerife, Canary Islands. *Lithos* **32**, 1–19.

Bachmann, O. & Bergantz, G. (2004). On the origin of crystal-poor rhyolites: extracted from batholithic crystal mushes. *Journal of Petrology* **45**, 1565–1582.

Bachmann, O. & Bergantz, G. W. (2008). Deciphering magma chamber dynamics from styles of compositional zoning in large silicic ash flow sheets. In: Putirka, K. D. & Tepley, F. J., III (eds) *Minerals, Inclusions and Volcanic Processes. Mineralogical Society of America and Geochemical Society, Reviews in Mineralogy and Geochemistry* **69**, 651–674.

Bachmann, O., Oberli, F., Dungan, M., Meier, M., Mundil, R. & Fischer, H. (2007). $^{40}Ar/^{39}Ar$ and U–Pb dating of the Fish Canyon magmatic system, San Juan Volcanic field, Colorado: Evidence for an extended crystallization history. *Chemical Geology* **236**, 134–166.

Bachmann, O., Deering, C. D., Lipman, P. W. & Plummer, C. (2014). Building zoned ignimbrites by recycling silicic cumulates: insight from the 1,000 km^3 Carpenter Ridge Tuff, CO. *Contributions to Mineralogy and Petrology* **167**, 1–13.

Bacon, C. R. & Druitt, T. H. (1988). Compositional evolution of the zoned calcalkaline magma chamber of Mount Mazama, Crater Lake, Oregon. *Contributions to Mineralogy and Petrology* **98**, 224–256.

Bohrson, W. A., Spera, F. J., Fowler, S. J., Belkin, H. E., De Vivo, B. & Rolandi, G. (2006). Petrogenesis of the Campanian ignimbrite: implications for crystal–melt separation and open-system processes from major and trace elements and Th isotopic data. *Developments in Volcanology* **9**, 249–288.

Brändle, J. & Santín, S. F. (1979). On the non-existence of a tholeiitic series in the Canary Islands. *Chemical Geology* **26**, 91–103.

Brophy, J. (1991). Composition gaps, critical crystallinity, and fractional crystallization in orogenic (calc-alkaline) magmatic systems. *Contributions to Mineralogy and Petrology* **109**, 173–182.

Brown, S. J. & Fletcher, I. R. (1999). SHRIMP U–Pb dating of the preeruption growth history of zircons from the 340 ka Whakamaru Ignimbrite, New Zealand: Evidence for >250 ky magma residence times. *Geology* **27**, 1035–1038.

Brown, R., Barry, T., Branney, M., Pringle, M. & Bryan, S. (2003). The Quaternary pyroclastic succession of southeast Tenerife, Canary Islands: explosive eruptions, related caldera subsidence, and sector collapse. *Geological Magazine* **140**, 265–288.

Bryan, S. (2006). Petrology and geochemistry of the Quaternary caldera-forming, phonolitic Granadilla eruption, Tenerife (Canary Islands). *Journal of Petrology* **47**, 1557–1589.

Bryan, S., Martí, J. & Cas, R. (1998). Stratigraphy of the Bandas del Sur Formation: an extracaldera record of Quaternary phonolitic explosive eruptions from the Las Cañadas edifice, Tenerife (Canary Islands). *Geological Magazine* **135**, 605–636.

Bryan, S., Marti, J. & Leosson, M. (2002). Petrology and geochemistry of the Bandas del Sur Formation, Las Cañadas edifice, Tenerife (Canary Islands). *Journal of Petrology* **43**, 1815–1856.

Bunsen, R. (1851). Ueber die Processe der vulkanischen Gesteinsbildungen Islands. *Annalen der Physik* **159**, 197–272.

Burgisser, A. & Bergantz, G. W. (2011). A rapid mechanism to remobilize and homogenize highly crystalline magma bodies. *Nature* **471**, 212–215.

Burgisser, A., Bergantz, G. W. & Breidenthal, R. E. (2005). Addressing complexity in laboratory experiments: the scaling of dilute multiphase flows in magmatic systems. *Journal of Volcanology and Geothermal Research* **141**, 245–265.

Carracedo, J. (1994). The Canary Islands: an example of structural control on the growth of large oceanic-island volcanoes. *Journal of Volcanology and Geothermal Research* **60**, 225–241.

Carracedo, J. (1999). Growth, structure, instability and collapse of Canarian volcanoes and comparisons with Hawaiian volcanoes. *Journal of Volcanology and Geothermal Research* **94**, 1–19.

Carracedo, J., Badiola, E. R., Guillou, H., Paterne, M., Scaillet, S., Torrado, F. P., Paris, R., Fra-Paleo, U. & Hansen, A. (2007). Eruptive and structural history of Teide Volcano and rift zones of Tenerife, Canary Islands. *Geological Society of America Bulletin* **119**, 1027–1051.

Carracedo, J., Guillou, H., Nomade, S., Rodríguez-Badiola, E., Pérez-Torrado, F., Rodríguez-González, A., Paris, R., Troll, V., Wiesmaier, S. & Delcamp, A. (2011). Evolution of ocean-island rifts: the northeast rift zone of Tenerife, Canary Islands. *Geological Society of America Bulletin* **123**, 562–584.

Charlier, B., Wilson, C., Lowenstern, J., Blake, S., Van Calsteren, P. & Davidson, J. (2005). Magma generation at a large, hyperactive silicic volcano (Taupo, New Zealand) revealed by U–Th and U–Pb systematics in zircons. *Journal of Petrology* **46**, 3–32.

Chayes, F. (1963). Relative abundance of intermediate members of the oceanic basalt-trachyte association. *Journal of Geophysical Research* **68**, 1519–1534.

Costa, F. (2008). Residence times of silicic magmas associated with calderas. *Developments in Volcanology* **10**, 1–55.

Daly, R. A. (1925). The geology of Ascension Island. *Proceedings of the American Academy of Arts and Sciences* **60**, 3–80.

Dávila-Harris, P. (2009). Explosive ocean-island volcanism: the 1·8–0·7 Ma explosive eruption history of Cañadas volcano recorded by the pyroclastic successions around Adeje and Abona, southern Tenerife, Canary Islands. University of Leicester.

Dávila-Harris, P., Ellis, B., Branney, M. & Carrasco-Núñez, G. (2013). Lithostratigraphic analysis and geochemistry of a vitric spatter-bearing ignimbrite: the Quaternary Adeje Formation, Cañadas volcano, Tenerife (Doctoral dissertation). *Bulletin of Volcanology* **75**, 1–15.

Davis, R. H. & Acrivos, A. (1985). Sedimentation of noncolloidal particles at low Reynolds numbers. *Annual Review of Fluid Mechanics* **17**, 91–118.

Deering, C., Bachmann, O. & Vogel, T. (2011). The Ammonia Tanks Tuff: Erupting a melt-rich rhyolite cap and its remobilized crystal cumulate. *Earth and Planetary Science Letters* **310**, 518–525.

DePaolo, D. (1981). Trace element and isotopic effects of combined wallrock assimilation and fractional crystallization. *Earth and Planetary Science Letters* **53**, 189–202.

Dufek, J. & Bachmann, O. (2010). Quantum magmatism: Magmatic compositional gaps generated by melt–crystal dynamics. *Geology* **38**, 687–690.

Edgar, C., Wolff, J., Nichols, H., Cas, R. & Martí, J. (2002). A complex Quaternary ignimbrite-forming phonolitic eruption: the Poris member of the Diego Hernández Formation (Tenerife, Canary Islands). *Journal of Volcanology and Geothermal Research* **118**, 99–130.

Edgar, C., Wolff, J., Olin, P., Nichols, H., Pittari, A., Cas, R., Reiners, P., Spell, T. & Martí, J. (2007). The late Quaternary Diego Hernandez Formation, Tenerife: Volcanology of a complex cycle of voluminous explosive phonolitic eruptions. *Journal of Volcanology and Geothermal Research* **160**, 59–85.

Ellis, B. S., Bachmann, O. & Wolff, J. A. (2014). Cumulate fragments in silicic ignimbrites: The case of the Snake River Plain. *Geology* **42**, 431–434.

Evans, B. W. & Bachmann, O. (2013). Letter: Implications of equilibrium and disequilibrium among crystal phases in the Bishop Tuff. *American Mineralogist* **98**, 271–274.

Fowler, S. J., Spera, F. J., Bohrson, W. A., Belkin, H. E. & De Vivo, B. (2007). Phase equilibria constraints on the chemical and physical evolution of the Campanian Ignimbrite. *Journal of Petrology* **48**, 459–493.

Freundt-Malecha, B., Schmincke, H.U. & Freundt, A. (2001). Plutonic rocks of intermediate composition on Gran Canaria: the missing link of the bimodal volcanic rock suite. *Contributions to Mineralogy and Petrology* **141**, 430–445.

Gelman, S. E., Gutiérrez, F. J. & Bachmann, O. (2013). On the longevity of large upper crustal silicic magma reservoirs. *Geology* **41**, 759–762.

Gualda, G. A., Ghiorso, M. S., Lemons, R. V. & Carley, T. L. (2012). Rhyolite-MELTS: a modified calibration of MELTS optimized for silica-rich, fluid-bearing magmatic systems. *Journal of Petrology* **53**, 875–890.

Guillong, M., Meier, D., Allan, M., Heinrich, C. & Yardley, B. (2008). SILLS: a MATLAB-based program for the reduction of laser ablation ICP-MS data of homogeneous materials and inclusions. In: Sylvester, P. (ed.), Laser-Ablation-ICP-MS in the Earth Sciences, Current Practices and Outstanding Issues, *Mineralogical Association of Canada Short Course* **40**, 328–333.

Gurenko, A., Hoernle, K., Hauff, F., Schmincke, H., Han, D., Miura, Y. & Kaneoka, I. (2006). Major, trace element and Nd–Sr–Pb–O–He–Ar isotope signatures of shield stage lavas from the central and western Canary Islands: insights into mantle and crustal processes. *Chemical Geology* **233**, 75–112.

Hildreth, W. (1979). The Bishop Tuff: Evidence for the origin of compositional zonation in silicic magma chambers. In: Chapin, C. & Elston, W. (eds), Ash Flow Tuffs, *Geological Society of America, Special Papers* **180**, 43–75.

Hildreth, W. & Wilson, C. J. (2007). Compositional zoning of the Bishop Tuff. *Journal of Petrology* **48**, 951–999.

Hoernle, K. (1998). Geochemistry of Jurassic oceanic crust beneath Gran Canaria (Canary Islands): implications for crustal recycling and assimilation. *Journal of Petrology* **39**, 859–880.

Hoernle, K., Tilton, G. & Schmincke, H. (1991). Sr–Nd–Pb isotopic evolution of Gran Canaria: Evidence for shallow enriched mantle beneath the Canary Islands. *Earth and Planetary Science Letters* **106**, 44–63.

Huber, C., Bachmann, O. & Manga, M. (2009). Homogenization processes in silicic magma chambers by stirring and mushification (latent heat buffering). *Earth and Planetary Science Letters* **283**, 38–47.

Huber, C., Bachmann, O. & Dufek, J. (2011). Thermo-mechanical reactivation of locked crystal mushes: Melting-induced internal fracturing and assimilation processes in magmas. *Earth and Planetary Science Letters* **304**, 443–454.

Huertas, M., Arnaud, N., Ancochea, E., Cantagrel, J. M. & Fúster, J. (2002). $^{40}Ar/^{39}Ar$ stratigraphy of pyroclastic units from the Canadas volcanic edifice (Tenerife, Canary Islands) and their bearing on the structural evolution. *Journal of Volcanology and Geothermal Research* **115**, 351–365.

Ibarrola, E. (1969). Variation trends in basaltic rocks of the Canary Islands. *Bulletin of Volcanology* **33**, 729–777.

Jarosewich, E., Nelen, J. & Norberg, J. A. (1980). Reference samples for electron microprobe analysis. *Geostandards Newsletter* **4**, 43–47.

Karakas, O. & Dufek, J. (2015). Melt evolution and residence in extending crust: Thermal modeling of the crust and crustal magmas. *Earth and Planetary Science Letters* **425**, 131–144.

Klügel, A., Hansteen, T. H. & Galipp, K. (2005). Magma storage and underplating beneath Cumbre Vieja volcano, La Palma (Canary Islands). *Earth and Planetary Science Letters* **236**, 211–226.

Koyaguchi, T. & Kaneko, K. (1999). A two-stage thermal evolution model of magmas in continental crust. *Journal of Petrology* **40**, 241–254.

Krastel, S. & Schmincke, H. (2002). Crustal structure of northern Gran Canaria, Canary Islands, deduced from active seismic tomography. *Journal of Volcanology and Geothermal Research* **115**, 153–177.

Le Bas, M., Le Maitre, R., Streckeisen, A. & Zanettin, B. (1986). A chemical classification of volcanic rocks based on the total alkali–silica diagram. *Journal of Petrology* **27**, 745–750.

Lee, C.-T. A. & Bachmann, O. (2014). How important is the role of crystal fractionation in making intermediate magmas? Insights from Zr and P systematics. *Earth and Planetary Science Letters* **393**, 266–274.

Lipman, P. W. (1966). Water pressures during differentiation and crystallization of some ash-flow magmas from southern Nevada. *American Journal of Science* **264**, 810–826.

Lipman, P. W. & Mehnert, H. H. (1975). Late Cenozoic basaltic volcanism and development of the Rio Grande depression in the southern Rocky Mountains. In: Curtis, B. (ed.), Cenozoic History of the Southern Rocky Mountains, *Geological Society of America, Memoirs* **144**, 119–154.

Lipman, P. W., Doe, B. R., Hedge, C. E. & Steven, T. A. (1978). Petrologic evolution of the San Juan volcanic field, southwestern Colorado: Pb and Sr isotope evidence. *Geological Society of America Bulletin* **89**, 59–82.

Mancini, A., Mattsson, H. B. & Bachmann, O. (2015). Origin of the compositional diversity in the basalt-to-dacite series erupted along the Heiðarsporður ridge, NE Iceland. *Journal of Volcanology and Geothermal Research* **301**, 116–127.

Marsh, B. (1981). On the crystallinity, probability of occurrence, and rheology of lava and magma. *Contributions to Mineralogy and Petrology* **78**, 85–98.

Martí, J., Mitjavila, J. & Araña, V. (1994). Stratigraphy, structure and geochronology of the Las Cañadas caldera (Tenerife, Canary Islands). *Age* **40**, T7.

McDonough, W. F. & Sun, S.-S. (1995). The composition of the Earth. *Chemical Geology* **120**, 223–253.

Morse, S. (2011). The fractional latent heat of crystallizing magmas. *American Mineralogist* **96**, 682–689.

Nash, W. & Crecraft, H. (1985). Partition coefficients for trace elements in silicic magmas. *Geochimica et Cosmochimica Acta* **49**, 2309–2322.

Neumann, E., Wulff-Pedersen, E., Simonsen, S., Pearson, N., Martí, J. & Mitjavila, J. (1999). Evidence for fractional crystallization of periodically refilled magma chambers in Tenerife, Canary Islands. *Journal of Petrology* **40**, 1089–1123.

Nichols, H. J. (2001). Petrologic and geochemical variation of a caldera-forming ignimbrite: the Abrigo Member, Diego Hernández Formation, Tenerife, Canary Islands (Spain). (MSc Thesis). Washington State University.

Pamukcu, A. S., Carley, T. L., Gualda, G. A., Miller, C. F. & Ferguson, C. A. (2013). The evolution of the Peach Spring giant magma body: Evidence from accessory mineral textures and compositions, bulk pumice and glass geochemistry, and rhyolite-MELTS modeling. *Journal of Petrology* **54**, 1109–1148.

Reid, M. R., Coath, C. D., Harrison, T. M. & McKeegan, K. D. (1997). Prolonged residence times for the youngest rhyolites associated with Long Valley Caldera: $^{230}Th–^{238}U$ ion microprobe dating of young zircons. *Earth and Planetary Science Letters* **150**, 27–39.

Ridley, W. (1970). The petrology of the Las Canadas volcanoes, Tenerife, Canary islands. *Contributions to Mineralogy and Petrology* **26**, 124–160.

Robertson, A. & Stillman, C. (1979). Late Mesozoic sedimentary rocks of Fuerteventura, Canary Islands: implications for West African continental margin evolution. *Journal of the Geological Society, London* **136**, 47–60.

Rooney, T. O., Hart, W. K., Hall, C. M., Ayalew, D., Ghiorso, M. S., Hidalgo, P. & Yirgu, G. (2012). Peralkaline magma evolution and the tephra record in the Ethiopian Rift. *Contributions to Mineralogy and Petrology* **164**, 407–426.

Saar, M. O., Manga, M., Cashman, K. V. & Fremouw, S. (2001). Numerical models of the onset of yield strength in crystal–melt suspensions. *Earth and Planetary Science Letters* **187**, 367–379.

Sarbas, B. & Nohl, U. (2008). The GEOROC database as part of a growing geoinformatics network. Presented at Geoinformatics Conference, Potsdam, 2008, Paper No. 4–3.

Schmincke, H.-U. (1976). The geology of the Canary Islands. In: Kunkel, G. (ed.), *Biogeography and Ecology in the Canary Islands*. Springer, pp. 67–184.

Schmitt, A. K., Lindsay, J. M., de Silva, S. & Trumbull, R. B. (2003). U–Pb zircon chronostratigraphy of early-Pliocene ignimbrites from La Pacana, north Chile: implications for the formation of stratified magma chambers. *Journal of Volcanology and Geothermal Research* **120**, 43–53.

Sigurdsson, H. & Sparks, R. (1981). Petrology of rhyolitic and mixed magma ejecta from the 1875 eruption of Askja, Iceland. *Journal of Petrology* **22**, 41–84.

Simon, J. I., Renne, P. R. & Mundil, R. (2008). Implications of pre-eruptive magmatic histories of zircons for U–Pb geochronology of silicic extrusions. *Earth and Planetary Science Letters* **266**, 182–194.

Sparks, R. S. J. & Marshall, L. A. (1986). Thermal and mechanical constraints on mixing between mafic and silicic magmas. *Journal of Volcanology and Geothermal Research* **29**, 99–124.

Szymanowski, D., Ellis, B. S., Bachmann, O., Guillong, M. & Phillips, W. M. (2015). Bridging basalts and rhyolites in the Yellowstone–Snake River Plain volcanic province: The elusive intermediate step. *Earth and Planetary Science Letters* **415**, 80–89.

Taylor, H. (1980). The effects of assimilation of country rocks by magmas on $^{18}O/^{16}O$ and $^{87}Sr/^{86}Sr$ systematics in igneous rocks. *Earth and Planetary Science Letters* **47**, 243–254.

Thirlwall, M., Singer, B. & Marriner, G. (2000). ^{39}Ar–^{40}Ar ages and geochemistry of the basaltic shield stage of Tenerife, Canary Islands, Spain. *Journal of Volcanology and Geothermal Research* **103**, 247–297.

Triebold, S., Kronz, A. & Wörner, G. (2006). Anorthite-calibrated backscattered electron profiles, trace elements, and growth textures in feldspars from the Teide–Pico Viejo volcanic complex (Tenerife). *Journal of Volcanology and Geothermal Research* **154**, 117–130.

Villemant, B. (1988). Trace element evolution in the Phlegrean Fields (Central Italy): fractional crystallization and selective enrichment. *Contributions to Mineralogy and Petrology* **98**, 169–183.

Wade, J. A., Plank, T., Stern, R.J., et al. (2005). The May 2003 eruption of Anatahan volcano, Mariana Islands: geochemical evolution of a silicic island-arc volcano. *Journal of Volcanology and Geothermal Research* **146**, 139–170.

Whitney, D. L. & Evans, B. W. (2010). Abbreviations for names of rock-forming minerals. *American Mineralogist* **95**, 185–187.

Wiesmaier, S., Troll, V., Carracedo, J., Ellam, R., Bindeman, I. & Wolff, J. (2012). Bimodality of lavas in the Teide–Pico Viejo succession in Tenerife—the role of crustal melting in the origin of recent phonolites. *Journal of Petrology* **53**, 2465–2495.

Wiesmaier, S., Troll, V., Wolff, J. & Carracedo, J. (2013). Open-system processes in the differentiation of mafic magma in the Teide–Pico Viejo succession, Tenerife. *Journal of the Geological Society, London* **170**, 557–570.

Wolff, J. (1985). Zonation, mixing and eruption of silica-undersaturated alkaline magma: a case study from Tenerife, Canary Islands. *Geological Magazine* **122**, 623–640.

Wolff, J. & Palacz, Z. (1989). Lead isotope and trace element variation in Tenerife pumices: evidence for recycling within an ocean island volcano. *Mineralogical Magazine* **53**, 519–525.

Wolff, J. & Storey, M. (1984). Zoning in highly alkaline magma bodies. *Geological Magazine* **121**, 563–575.

Wolff, J., Wörner, G. & Blake, S. (1990). Gradients in physical parameters in zoned felsic magma bodies: implications for evolution and eruptive withdrawal. *Journal of Volcanology and Geothermal Research* **43**, 37–55.

Wolff, J., Grandy, J. & Larson, P. (2000). Interaction of mantle-derived magma with island crust? Trace element and oxygen isotope data from the Diego Hernandez Formation, Las Cañadas, Tenerife. *Journal of Volcanology and Geothermal Research* **103**, 343–366.

Wolff, J., Ellis, B., Ramos, F., Starkel, W., Boroughs, S., Olin, P. & Bachmann, O. (2015). Remelting of cumulates as a process for producing chemical zoning in silicic tuffs: A comparison of cool, wet and hot, dry rhyolitic magma systems. *Lithos* **236**, 275–286.

Wolff, J. A. (1987). Crystallisation of nepheline syenite in a subvolcanic magma system: Tenerife, Canary Islands. *Lithos* **20**, 207–223.

Wörner, G. & Wright, T. L. (1984). Evidence for magma mixing within the Laacher See magma chamber (East Eifel, Germany). *Journal of Volcanology and Geothermal Research* **22**, 301–327.

Wörner, G. & Schmincke, H. (1984). Mineralogical and chemical zonation of the Laacher See tephra sequence (East Eifel, W. Germany). *Journal of Petrology* **25**, 805–835.

Wörner, G., Beusen, J.-M., Duchateau, N., Gijbels, R. & Schmincke, H.-U. (1983). Trace element abundances and mineral/melt distribution coefficients in phonolites from the Laacher See Volcano (Germany). *Contributions to Mineralogy and Petrology* **84**, 152–173.

Ye, S., Canales, J., Rihm, R., Danobeitia, J. & Gallart, J. (1999). A crustal transect through the northern and northeastern part of the volcanic edifice of Gran Canaria, Canary Islands. *Journal of Geodynamics* **28**, 3–26.